UNIVERSITY OF OKLAHOMA
GRADUATE COLLEGE

SHARPNESS BASED AUTOFOCUS FOR NON-COOPERATIVE MOVING TARGETS IN SAR DATA

A THESIS
SUBMITTED TO THE GRADUATE FACULTY
in partial fulfillment of the requirements for the
Degree of
MASTER OF SCIENCE

By
CALEB NELSON
Norman, Oklahoma
2026

SHARPNESS BASED AUTOFOCUS FOR NON-COOPERATIVE MOVING TARGETS IN SAR DATA

A THESIS APPROVED FOR THE
SCHOOL OF ELECTRICAL AND COMPUTER ENGINEERING

BY THE COMMITTEE CONSISTING OF

Dr. Nathan Goodman, Chair

Dr. Justin Metcalf

Dr. Russell Kenney

Table of Contents

List of Figures

List of Tables

Abstract

Synthetic aperture radar (SAR) imaging of stationary scenes relies on known geometry to form focused images. When a distributed target is moving, the mismatch between assumed and actual target kinematics causes displacement and blur of the target in the image. While various inverse SAR (ISAR) autofocus techniques exist that compensate for target motion, each is tailored to specific operational constraints. This thesis proposes a parametric image-sharpness-based autofocus technique for ground-based non-cooperative moving targets, using the backprojection algorithm. The proposed approach presents motion compensation as a two-parameter image sharpness optimization over target range acceleration and rotation rate. Translational motion compensation (TMC) is first achieved by integrating along the target's slow-time range profile via a range-acceleration search. Subsequently, rotational motion compensation (RMC) addresses target rotation relative to the radar through a rotation-rate search. The proposed method is validated on synthetic SAR data and applied to measured data.

Chapter 1

Introduction

1.1 Motivation

Synthetic aperture radar (SAR) is a remote sensing technology used to form images from aircraft or spacecraft. Unlike optical imaging systems, SAR uses radio-frequency electromagnetic waves rather than the visible spectrum. SAR offers advantages in adverse weather conditions and at night. Optical cameras rely on external light sources and require clear weather. SAR, on the other hand, is self-illuminating and weakly attenuated by clouds and rain. These advantages make SAR a helpful tool for surveillance and reconnaissance.

SAR images can look similar to grayscale optical images, but they have distinct differences in image formation. The SAR image formation process requires knowledge of the relative motion of the target scene with respect to the radar. If a target's motion does not match that of the target scene, the image of the scene will distort or shift. This issue becomes evident when a ground-moving target is present. A moving target's motion will not match the model for stationary ground objects. This mismatch results in translation or smearing of the target energy in the image [1].

Energy displacement and smearing pose a problem for locating and focusing a moving target. The motivation for this work is to focus the target energy and estimate its motion parameters. This is accomplished using a parametric, image-sharpness-based autofocus technique.

1.2 Background

Standard autofocus techniques aim to compensate for phase errors that reduce image quality. These errors may be caused by uncompensated motion, hardware limitations, algorithmic approximations, or propagation effects. Many traditional SAR autofocus algorithms such as map drift [2, 3], phase difference autofocus [4], and phase gradient autofocus (PGA) [5] are space-invariant. The phase error compensation in these algorithms is equally applied to all scatterers in the image [4]. Space-invariant phase error correction is suitable when the errors are caused by uncompensated platform motion. However, when a moving target is present in the data, the phase errors associated with that target differ from those of the rest of the image. The phase error unique to the target must instead be estimated. This error estimation is difficult in the presence of clutter [6].

A moving target in a scene with unknown motion parameters is called a non-cooperative moving target. Some techniques for imaging non-cooperative movers are classified as Inverse Synthetic Aperture Radar (ISAR). An imaging technique is classified as ISAR when the aperture is created from the changing position of a moving target rather than a moving radar platform [7]. ISAR imaging was originally proposed after experiments to image a vehicle on a turntable with a static radar. The method used to account for target motion is situation-dependent. Most well-defined ISAR techniques were designed for focusing aircraft or sea vessels [6].

Target motion includes both rotation and translation. Consequently, the ISAR focusing process can be broken into two parts: translational motion compensation (TMC) and rotational motion compensation (RMC) [8]. Some existing methods for translational motion compensation are accomplished in two steps. The first step is coarse motion compensation via range alignment. Range alignment can be accomplished by one of several methods: cross-correlation between envelopes of two range profiles [9]; range centroid alignment, which utilizes a center of mass calculation for each profile [10, 11]; entropy function minimization, which evaluates the probability distribution function of range bins [12, 13, 14, 15]; or by some other cost function [6]. The next step is a phase alignment for fine motion compensation. Fine motion compensation can be accomplished through a phase gradient autofocus (PGA) [16], Doppler centroid alignment [11], entropy minimization [17], or through some other cost function, such as contrast optimization [18] or variance minimization [19].

Rotational motion compensation (RMC) is performed after TMC. RMC is also often split into two parts: image reconstruction filtering and cross-range scaling. Simple range-Doppler (RD) algorithms are rarely used and do not produce sufficient results. The keystone formatting method is often rejected as well because it can only account for a single order of scatterer motion [8, 20]. Common image reconstruction methods use time-frequency representations (TFRs) [21, 22]. These methods are often referred to as Range instantaneous Doppler (RID) methods to distinguish them from RD algorithms. The ISAR Polar Format Algorithm can also be applied with some hypothesized rotation [23]. The optimal rotation rate is often found via an entropy minimization [6, 8].

Algorithms applied in ISAR autofocus include Prominent Point Processing (PPP) [1], PGA, image contrast-based autofocus (ICBA) [24], and entropy minimization-based autofocus (EMBA) [12, 25]. PPP requires multiple prominent points on the target of interest to estimate phase errors [9]. A small target, such as a car, may not have multiple prominent points to perform PPP. The PGA algorithm may be suitable for focusing the vehicle; however, it is a non-parametric autofocus, which complicates target motion estimation. EMBA attempts to estimate the optimal phase function that minimizes the image 2-D entropy cost function [14, 26]. This method is suitable for focusing a small target, but the target's motion parameters are not immediately evident once the optimal phase function has been found. The last technique, ICBA, is a parameter-based search that evaluates image quality based on motion hypotheses [6]. ICBA requires that the target signal power in the image be greater than the clutter power, but the parametric nature of ICBA makes it a desirable approach for this work. The proposed autofocus technique in this thesis is similar in structure to the ICBA algorithm.

1.3 Contributions

In this work, a backprojection-based ISAR parametric autofocus technique utilizing an image sharpness metric has been developed and successfully implemented on simulated and real SAR data. A moving target is focused by searching for the combination of range acceleration and rotation rate that produces the maximally sharp image. In Chapter 2, the SAR signal model and the backprojection image formation method are reviewed. Chapter 3 discusses the effects of a non-cooperative moving target on the target's appearance in a SAR image. This chapter demonstrates that a target's cross-range velocity manifests as a range acceleration in the SAR phase history. Chapter 4 explains the proposed autofocus technique and its implementation in detail. In Chapter 5, the results of the algorithm are shown. Some of the analysis conducted during the development of this algorithm is also shown in

Chapter 5, including the development of a cross-range scaling method that accounts for target rotation-dependent azimuth resolution.

Chapter 2

SAR Image Theory

2.1 SAR Background

Radar was originally an acronym for RAdio Detection and Ranging. Developed in the early twentieth century, this technology was employed to detect ships and aircraft. The British Chain Home radar network was notably used during World War II as an early warning against German air raids [3].

A conventional radar's cross-range resolution depends on the antenna's aperture [3]. The aperture of an antenna refers to its effective width. Larger apertures produce finer resolution; however, perpetually increasing an antenna's size is impractical. This limitation restricts cross-range resolution, particularly for airborne systems with tighter size constraints. Synthetic aperture radar (SAR) offers a solution to this problem.

In June 1951, Carl Wiley of Goodyear Aircraft Corporation proposed the concept of SAR [4]. Though the antenna size remains fixed, a radar traveling along some path synthetically increases its aperture by collecting measurements from multiple locations along its flight path. The distance the system travels forms the radar's synthetic aperture [3]. The radar's cross-range resolution is related to the size of its aperture according to $R\lambda/D$, where λ is the transmitted wavelength, R is the range, and D is the aperture size [27, 28].

SAR is often used by the remote sensing community and offers some benefits over optical images [28]. Radar is self-illuminating, enabling it to operate day or night. The frequencies typically used for SAR are able to pass through clouds and rain, unlike optical frequencies [3, 28]. These benefits make SAR a useful surveillance tool.

There are several modes of SAR operation, including but not limited to Stripmap, Spotlight, Inverse, Bistatic, and Interferometric SAR [28]. We will emphasize the Spotlight SAR mode in this thesis. In this mode, the radar stays pointed at the same reference point for the whole duration of the synthetic aperture. A scene reference point (SRP) serves as the motion compensation point for the data. The range to this point is denoted as $R_0(m)$. The radar's position is precisely recorded pulse-to-pulse.

The radar transmits a structured pulse of electromagnetic radiation called a waveform. For convenience, we assume that the transmitted waveform is a Linear Frequency Modulated (LFM) chirp, which is commonly used in practice [3]. The transmitted LFM signal is given by

$$s_{LFM}(t) = a(t) \cos\left(2\pi F_{min} + \pi\gamma t^2\right), \tag{2.1}$$

where $a(t)$ is some windowed amplitude function that controls the duration of the pulse. The LFM starts at some frequency, F_{min} [Hz], and increases in frequency at a constant chirp rate, γ [Hz/s]. The chirp will last for a duration of time called the pulse width, T_p, in seconds. The waveform bandwidth is defined by $\beta = \gamma T_p$. The radar transmits this waveform and then listens for a period of time before transmitting another pulse. The time between pulses is called the pulse repetition interval

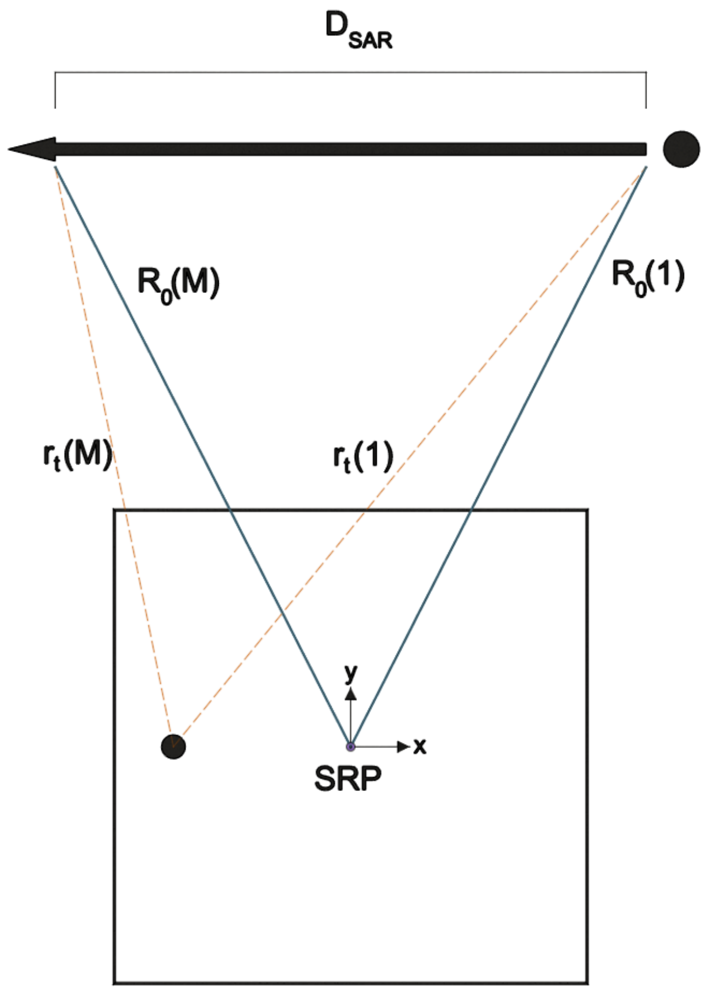

Figure 2.1: Simplified Spotlight SAR Geometry

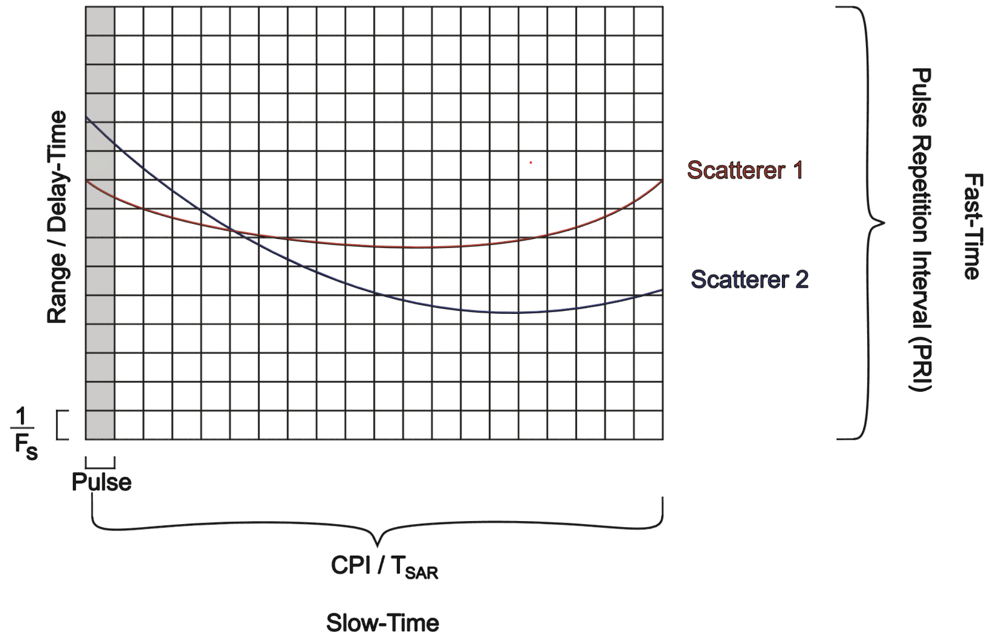

Figure 2.2: Radar data visualized by stacking measured pulses side by side. The Scatterers are intended to represent stationary objects on the ground.

(PRI). The data recorded from the pulse will be sampled at a specified frequency called the sample rate, F_s in samples per second. The measurement dimension corresponding to the listening period of a pulse is called fast time.

The transmitted pulse propagates through space, expanding with a spherical wavefront within the antenna beam width. The pulse impinges on objects in the illuminated scene and reflects back toward the radar. This reflected waveform is sampled and processed. The first step in processing is to pass the fast-time data for each pulse through a matched filter [3]. The matched filter is a time-reversed, conjugated copy of the waveform. The filtering can be done in the time domain as a convolution, or in the frequency domain via transforms and multiplication. The matched-filtering process is called pulse compression. The result is a time-delayed autocorrelation. After the filter is applied, peaks occur at time delays associated with reflections from the scene. The wave propagates at the speed of light, c, to a scatterer at range, r_t, and then returns to the radar. The delay time is based on the two-way propagation distance, such that

$$\tau_t = \frac{2r_t}{c}. \tag{2.2}$$

Matched filtering for wideband LFM waveforms is often implemented via a technique called stretch processing. When stretch processing is applied to a return from a particular scatterer, the returning chirp is mixed with a reference chirp centered at the operating frequency. The mixing process downconverts the signal to a single-frequency tone at baseband, commonly referred to as the beat frequency [4]. Because the linear frequency modulation has been removed, the signal is said to be deramped. The beat frequency is proportional to the scatterer's range. The ability to resolve the beat frequency, and thereby the range, is related to the pulse duration. The pulse duration for an LFM is proportional to the signal bandwidth. Radar range resolution is defined as [3]

$$\rho_R = \frac{c}{2\beta}. \tag{2.3}$$

As the SAR travels along its path, it creates a synthetic array. The illuminated scene is observed for duration T_{SAR} in seconds. The pulses received during this time span what is called the slow-time axis. The SAR cross-range resolution depends on the synthetic aperture rather than the physical aperture, wavelength, and range to the scene. The cross-range resolution achieved by the synthetic aperture [3] is given by

$$\rho_{CR} = \frac{\lambda R_0}{2D_{SAR}} = \frac{\lambda R_0}{2v_a T_{SAR}}, \tag{2.4}$$

where v_a is the platform velocity, D_{SAR} is the aperture size, and λ is the wavelength corresponding to the LFM's center frequency. High-resolution SAR datasets have wide bandwidths and long aperture times. We will now turn to the SAR signal model and the theory behind making an image with this data.

2.2 SAR Signal Model

The image formation process relies on observing the range migration of scatterers in the scene from pulse to pulse as the radar moves. To develop the signal model, we assume the signal from a scatterer is deramped. First, we define a scatterer's range from the antenna on each pulse. Let the radar antenna position, $\mathbf{p}_a$, and scatterer position, $\mathbf{p}_t$, for the *m*th pulse be defined as

$$\begin{aligned} \mathbf{p}_a(m) &= (x_a(m), y_a(m), z_a(m)), \\ \mathbf{p}_t(m) &= (x_t(m), y_t(m), z_t(m)). \end{aligned} \tag{2.5}$$

The scatterer range is then

$$r_t(m) = \sqrt{(x_t(m) - x_a(m))^2 + (y_t(m) - y_a(m))^2 + (z_t(m) - z_a(m))^2}. \tag{2.6}$$

In stretch processing, the received signal is mixed with a reference chirp centered at the SRP. This process simultaneously accomplishes frequency demodulation and removes the phase associated with the SRP. The complex, baseband, time-domain signal from a scatterer at range $r_t(m)$ on pulse m after stretch processing is given by [4]

$$s(t, m) = a_t \text{rect}\left(\frac{t - 2r_t(m)/c}{Tp}\right) \exp\left[\frac{-j4\pi\gamma}{c}\left(\frac{f_c}{\gamma} + t - \frac{2R_0(m)}{c}\right)\delta R_m\right], \tag{2.7}$$

where a_t is the received signal's complex amplitude, $\delta R_m = r_t(m) - R_0(m)$ is the differential range between the scatterer and the SRP, and f_c is the radar's center frequency [4, 29]. Next, we perform a change of variable to express the fast-time axis in terms of differential time to the scene reference point. The new term, $\hat{t}$, is given by $\hat{t} = t - 2R_0(m)/c$. The signal as a function of $\hat{t}$ is given by

$$s(\hat{t}, m) = a_t \text{rect}\left(\frac{\hat{t} - 2\delta R_m/c}{Tp}\right) \exp\left[\frac{-j4\pi\gamma}{c}\left(\frac{f_c}{\gamma} + \hat{t}\right)\delta R_m\right]. \tag{2.8}$$

Let ϕ_t represent the phase function of the signal given in (2.8). Before applying the Fourier Transform to (2.8), the phase expression is rearranged so that the time-dependent component has the same delay as the rectangular window. This step makes the Fourier Transform simpler to evaluate. The phase term is now given by

$$\phi_t(\hat{t}, m) = \left[\frac{-j4\pi\gamma}{c}\left(\left(\hat{t} - \frac{2\delta R_m}{c}\right) + \left(\frac{f_c}{\gamma} + \frac{2\delta R_m}{c}\right)\right)\delta R_m\right]. \tag{2.9}$$

The phase is now separated into a fast-time-dependent component and a pulse-dependent component. This step further simplifies the Fourier Transform because only the fast-time term contributes to the transform, while the pulse-dependent component remains a constant phase offset. The new expression is $\phi_t(\hat{t}, m) = \phi_{\hat{t}}(\hat{t}, m) + \phi_m(m)$, where

$$\begin{aligned} \phi_{\hat{t}}(\hat{t}, m) &= \left[-j\frac{4\pi\gamma}{c}\left(\hat{t} - \frac{2\delta R_m}{c}\right)\delta R_m\right], \text{ and} \\ \phi_m(m) &= \left[-j\frac{4\pi\gamma}{c}\left(\frac{f_c}{\gamma} + \frac{2\delta R_m}{c}\right)\delta R_m\right]. \end{aligned} \tag{2.10}$$

This signal is converted to range bins by a Fourier Transform (FT). The FT of $s(\hat{t}, m)$ is given by

$$S(F_{\hat{t}}, m) = a_t T_p \,\text{sinc}\left[T_p\left(F_{\hat{t}} + \gamma\frac{2\delta R_m}{c}\right)\right] \exp\left[-j\frac{4\pi}{c}\left(F_{\hat{t}} + \gamma\frac{2\delta R_m}{c}\right) + \phi_m(m)\right] \tag{2.11}$$

where $F_{\hat{t}}$ denotes the fast-time frequency (beat frequency) variable. Since beat frequency is proportional to differential range, the frequency variable can be substituted with its equivalent differential range, δr. The relationship between range and the peak output frequency after the FT is

$$F_{\hat{t}} = -\gamma \frac{2\delta r}{c}. \tag{2.12}$$

The signal can now be rewritten in terms of δr such that,

$$S(\delta r, m) = a_t T_p \operatorname{sinc}\left[-\beta \frac{2}{c}(\delta r - \delta R_m)\right] \exp\left[j \frac{8\pi\gamma}{c^2}(\delta r - \delta R_m)\delta R_m + \phi_m(m)\right]. \tag{2.13}$$

When the sampled differential range equals the scatterer's true differential range, $\delta r = \delta R_m$, the sinc function reaches its maximum, and the first term in the complex exponential goes to zero. In other words, when $S(\delta r, m)$ is sampled exactly corresponding to the target's differential range, this term will have no contribution to the signal phase. Consequently, the signal phase is determined solely by the pulse-dependent phase term, $\phi_m(m)$.

Turning attention to the second phase term in (2.13), $\phi_m(m)$ can be split into two terms: one corresponding to the target Doppler shift; and another that is an artifact of stretch processing called the range skew or residual video phase error (RVPE) [30]. Let $\phi_t(m) = \phi_D(m) + \phi_{RVPE}(m)$, where the terms are defined as

$$\begin{aligned} \phi_D(m) &= \left[-j \frac{4\pi f_c \delta R_m}{c}\right], \text{ and} \\ \phi_{RVPE}(m) &= \left[j \frac{8\pi\gamma\delta R_m^2}{c^2}\right]. \end{aligned} \tag{2.14}$$

The RVPE can degrade image quality if the differential range, δR_m, is sufficiently large. Both [4] and [30] present methods for deskewing the signal by removing this term. According to [4], this term is generally small and can be ignored without serious impact on image quality. In this thesis, we will only consider the impact of the Doppler term.

To evaluate the magnitude of a particular pixel in a SAR image, we must compensate for the Doppler phase term $\phi_D(m)$. Because the scatterer phase depends on the differential range, the phase compensation is equivalent to accounting for the scatter's range migration across pulses. This compensation is achieved by building a slow-time matched-filter for this scatterer pulse dependent range and . The matched filter integrates The relative range from the radar to the scatterer, $r_t(m)$, will be changing on a pulse-by-pulse basis as seen in Figure 2.1).

The matched filter response for a scatterer with the range profile $r_t(m)$ is given by [29]

$$Y(r_t) = \frac{1}{MK} \sum_{m=1}^{M} \sum_{k=1}^{K} S(\delta r, m) \exp\left[\frac{+j4\pi f_k \delta r}{c}\right], \qquad (2.15)$$

where K is the number of frequency samples, and M is the number of pulses.

SAR image grids assign x, y, and z positions to fixed pixels. The differential range for each pixel is calculated for every pulse to build its respective range profile. The image is formed by substituting the differential range profile δR_m into (2.15), then assigning the filter response magnitude to the associated pixel.

2.3 Backprojection Based Image Formation

The backprojection algorithm is a more efficient (albeit still computationally expensive) means of implementing the matched filter algorithm of (2.15). First, we return to the time-domain version of the scatterer's signal. The pulses will require a high fidelity range interpolation before the image forming process. The optimal method is a sinc interpolation, which can be approximated by zero-padding the deramped signal ($s(\hat{t}, m)$) before the DFT is applied [29, 30, 31]. Thus $S(\delta r, m)$ is the upsampled signal.

The steps to form the image are:

1. Define a pixelated image grid, including Coordinates.

2. Calculate the differential range to each pixel on the current pulse.

3. Interpolate the fast-time data for the current pulse to the ranges calculated in step #2.

4. Compensate for the phase term in (2.7) by multiplying with the conjugate of the phase.

5. Accumulate the values for each pixel into the image.

6. Progress to the next pulse and repeat Steps #2-#6 until all pulses have contributed to the image.

The image grid is defined by the $x,\ y,$ and z positions for each pixel. Let the Cartesian coordinate system have the origin as the SRP and let the plane defined by $z = 0$ coincide with the Earth's surface. Let $\mathbf{X}$, $\mathbf{Y}$, and $\mathbf{Z}$ be matrices that represent the $x,\ y,$ and z positions respectively of each pixel.

The differential range to each pixel on a pulse-by-pulse basis is given by

$$\delta R(i,j,m) = \sqrt{(\mathbf{X}(i,j) - x_a(m))^2 + (\mathbf{Y}(i,j) - y_a(m))^2 + (\mathbf{Z}(i,j) - z_a(m))^2} - R_0(m) \quad (2.16)$$

where i and j are the image pixel indices. The value of a particular pixel over the duration of the aperture time is given by

$$\mathbf{I}(i,j) = \sum_{m=1}^{M} S(\delta r', m) \exp\left[\frac{+j4\pi f_0 \delta R(i,j,m)}{c}\right], \tag{2.17}$$

where $s(\delta r', m)$ is the signal interpolated to the range corresponding to $\delta R(i,j,m)$. This step is repeated for all pixels to form your image. It is most efficient to perform this operation on all pixels in the image at one time before moving to the next pulse.

Chapter 3

Non-Cooperative Moving Targets in SAR Images

A non-cooperative Target is defined as a mover who is not communicating with the radar operator. There is no *a priori* knowledge of the target motion. To fully focus a target captured in SAR data, the targets motion with respect to the radar must be accounted for. If the target has movement that is unaccounted for, the final image will not accurately focus the target. This Chapter examines the impact of uncompensated motion on how a non-cooperative mover focuses in an image from the perspective of the backprojection algorithm.

3.1 Target Motion Model

Consider a rigid body whose motion is restricted to a plane. Its motion can be described by its ground velocity, ground acceleration, and rotation. The target will have a starting position $\mathbf{p}_t(1)$, a starting velocity $\mathbf{v}_t(1)$, and an acceleration $\mathbf{a}_t(m)$.

$$\mathbf{p}_t(1) = [x_t(1), y_t(1)] \tag{3.1}$$

$$\mathbf{v}_t(1) = [v_x(1), v_y(1)] \tag{3.2}$$

$$\mathbf{a}_t(m) = [a_x(m), a_y(m)]. \tag{3.3}$$

The position of the target on pulse m is defined as

$$\mathbf{p}_t(m) = \mathbf{p}_t(1) + \sum_{n=1}^{m} \left[\mathbf{v}_t(1) + \frac{1}{2} \sum_{k=1}^{n} \mathbf{a}_t(k) T(k) \right] T(n), \tag{3.4}$$

where $T(n)$ is the pulse repetition interval (PRI) for the current pulse index n or k.

The target's rotation is defined as a function of its velocity. The angular change of the velocity direction from m_1 to m_2 is the rotation that has been experienced about the rigid body center of rotation. The rotation angle (θ_t) between two pulses is defined as

$$\theta_t(m_1, m_2) = \arccos \frac{\langle \mathbf{v}_t(m_1), \mathbf{v}_t(m_2) \rangle}{|\mathbf{v}_t(m_1)||\mathbf{v}_t(m_2)|}. \tag{3.5}$$

Because the target is a rigid body and the translational motion is accounted for, the axis of rotation is defined in the z direction through the vehicle's center. This axis definition is only viable for a target whose change in direction requires a change in velocity, such as a car. A body that can rotate in place must be defined independently of the velocity vector.

Simulated SAR Scenario with a Mover

Since we are observing the target's motion with a single-channel radar, only the target's range on each pulse is observed. Because the target's motion is only observed in one dimension, some of the target's two- dimensional motion is not observed. The ability to construct a focused image will depend on tracking this target's range migration and rotation throughout the aperture time. Since it is a distributed target, each scatterer on the target will have its own range migration profile. There will be a mean range profile capturing the target's translational motion. The target's rotational motion manifests as a superposition of sinusoidal range-migration paths that center on the median range migration profile (Fig. 3.14).

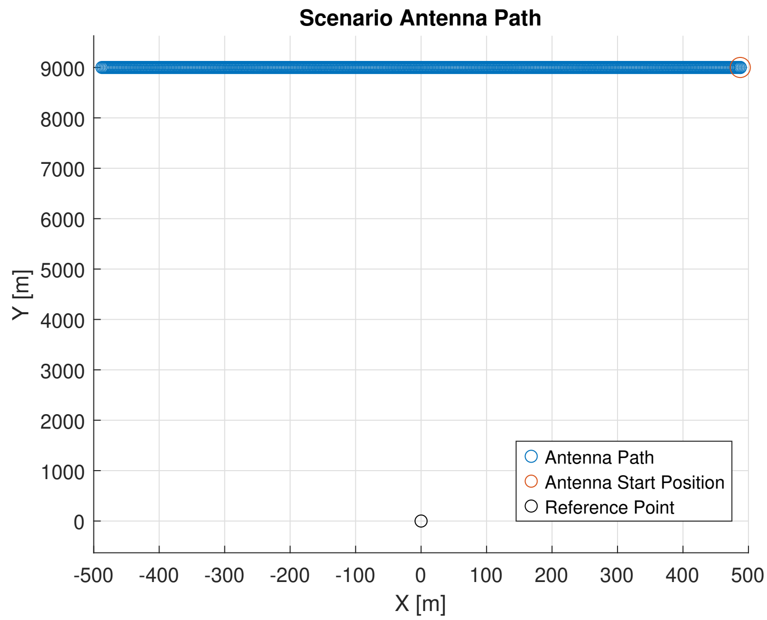

Figure 3.1: The flight path for the antenna in the scenario.

PRF	2400 [Hz]
Velocity	260 [m/s]
Pulses	9000

Table 3.1: Example SAR scenario parameters.

Consider the case where there are two point scatterers that are a part of the same rigid body. One scatterer is on the body's rotational axis, and the other is displaced by 2 meters (Fig. 3.2). The center of the rigid body on the first pulse has been chosen as the reference point for a SAR data collect. The antenna is flying a straight path in the negative x-direction. The range direction is being approximated as the positive y-direction, or the cross-track direction in this scenario.

To simplify the analysis, the system and the target motion are limited to the same plane. The system parameters are approximately the same as the GOTCHA collect discussed in Section 5.1.1. See table 3.1 for the example system parameters.

Three scenarios demonstrate the impact of cross-range velocity and rotation on

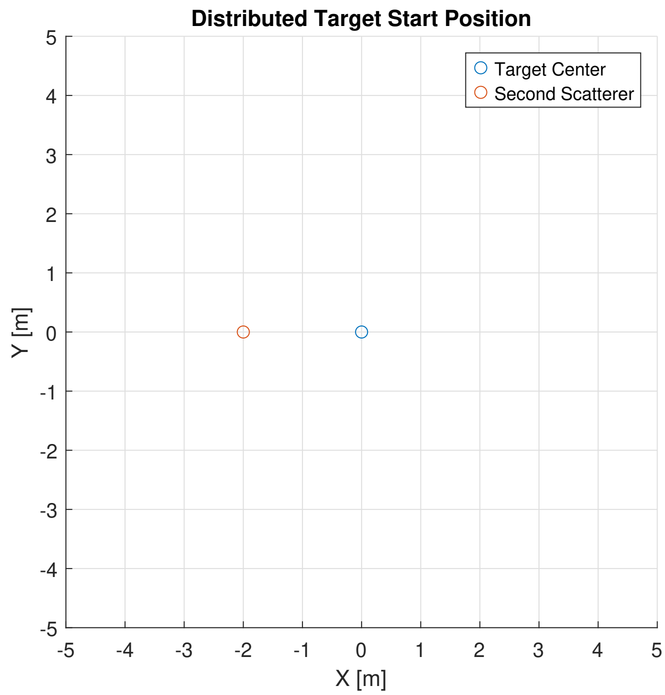

Figure 3.2: Point Scatterers on a rigid body.

the two scatterers' range migration across pulses. The following results from this experiment are used to justify the decisions made in Section 4.2. The first scenario is of the stationary scatterers, the second is with constant cross-range velocity, and the third is with constant rotational velocity.

The translational motion (eq. 3.4) of the target has been defined by some initial x and y position (eq. 3.1), x and y velocity (eq. 3.2), and x and y acceleration (eq. 3.3). However, from the radar's perspective, it only observes the target's range as a function of pulse number. The 2-D translational motion is reduced to a 1-D range profile. Let the range to the target be defined as

$$\begin{aligned} r_t(m) &= ||\mathbf{p}_t(m) - \mathbf{p}_a(m)|| \\ &= \sqrt{(x_t(m) - x_a(m))^2 + (y_t(m) - y_a(m))^2}, \end{aligned} \tag{3.6}$$

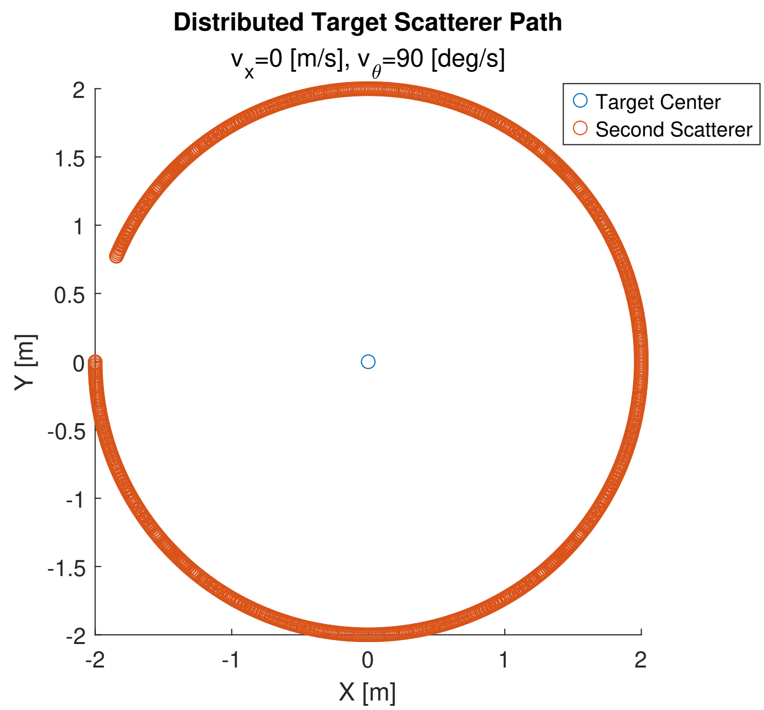

Figure 3.3: Path of the rigid body scatterers in the third scenario with no translational velocity and a constant rotational velocity of $90\,\deg/s$

where $x_a(m)$ and $y_a(m)$is the $x - y$ position of the antenna on pulse m. The 6 parameters needed to define the target translational motion on the ground are observed as a starting range, $r_t(1)$, a starting range velocity, $v_r(1)$, and a pulse-by-pulse range acceleration, $a_r(m)$.

3.2 Target Energy Displacement

The backprojection algorithm focuses stationary targets by integrating along their range-migration profile. The path is calculated using the known geometry of the ground scatterers relative to the platform. When a target has additional range velocity that distinguishes it from the stationary clutter around it, its range profile does not match the expected profile of its true location. The target energy construc-

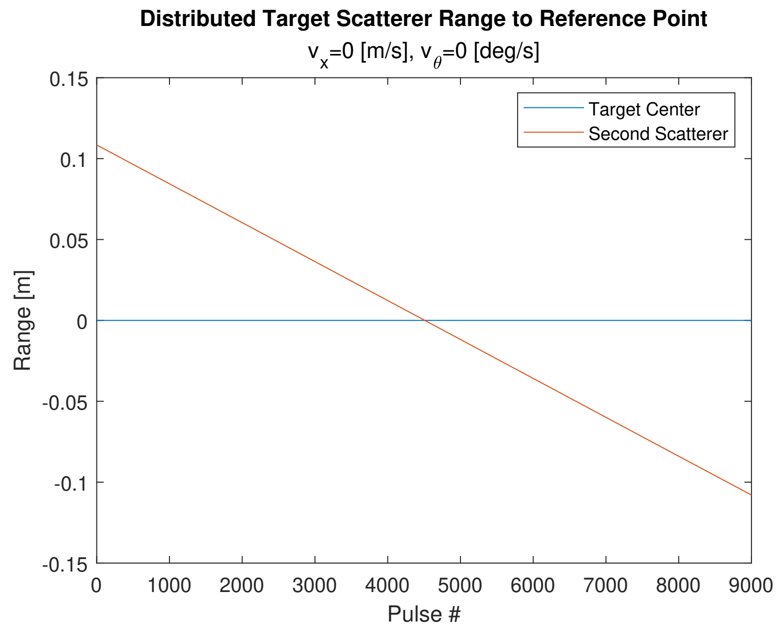

(a)

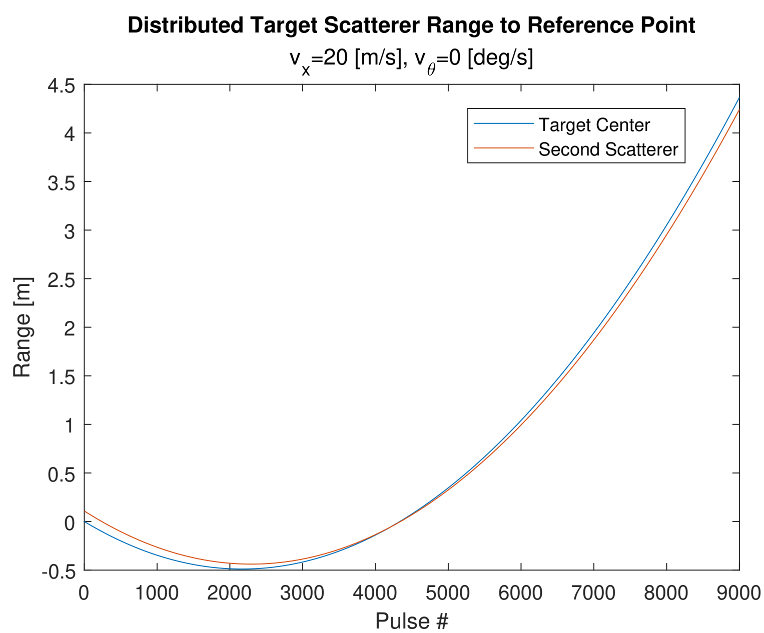

(b)

Figure 3.4: The range with respect to the scene reference point of the two scatterers in the rigid body scenarios. (a) with not translational or motion. (b) with purely cross-range motion. (c) with purely rotational motion.

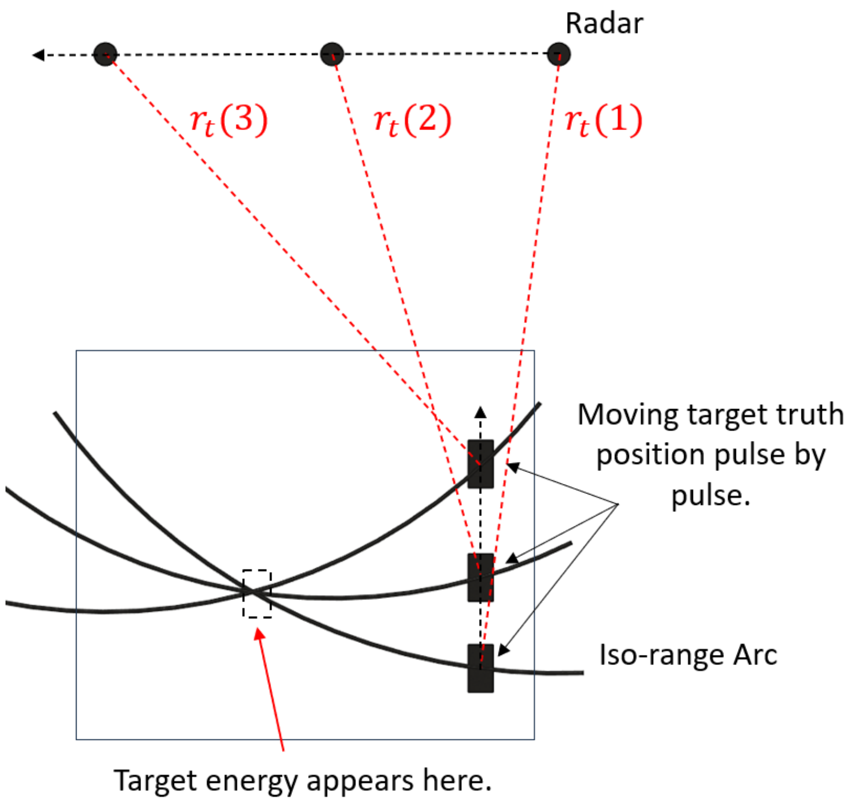

Figure 3.5: The moving target's energy is displaced because its range profile matches the range profile expected from pixels in a different part of the scene.

tively adds in a portion of the image where the range profiles of stationary pixels most highly correlate with the range profile of the target 3.5.

This target displacement makes it difficult to know the truth position of a target when there is only one antenna channel on the system. If the target's ground velocity is known, then the expected displacement due to that range velocity can be subtracted from its location in the image to estimate its true location in the scene. The approximate displacement is given by [32]

$$\Delta \mathbf{l}_t = -\frac{v_r R_0}{v_p} \hat{\mathbf{d}}_{\mathbf{CR}}, \tag{3.7}$$

where v_p is the radar velocity, R_0 is the range to the reference point, and $\hat{\mathbf{d}}_{CR}$ is

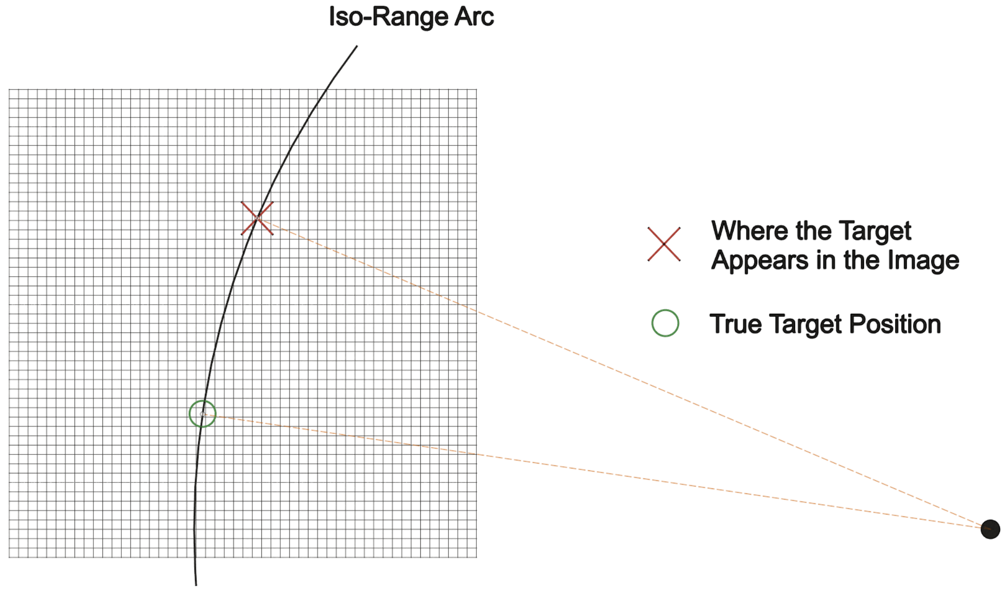

Figure 3.6: A moving target with some Doppler velocity will translate along an arc or constant range. The grid represents the image area.

the cross-range direction. The term v_r is the range velocity of the target minus the range velocity associated with its position. In other words, v_r is the ground velocity of the target projected onto the line-of-sight vector. The displacement occurs along the curve of constant range (Fig. 3.6). Over short distances (3.7) holds.

3.3 Target Blurring

Target blurring is caused by a target's motion that does not perfectly match any pixels in the image. The target's range profile does not perfectly match that of any pixel in the image. The target range profile may match that of one pixel for part of the observation interval, but diverge to match that of another pixel for another part of the interval. Major contributors to target smear are its range acceleration, cross-range velocity, and rotation rate [33, 34].

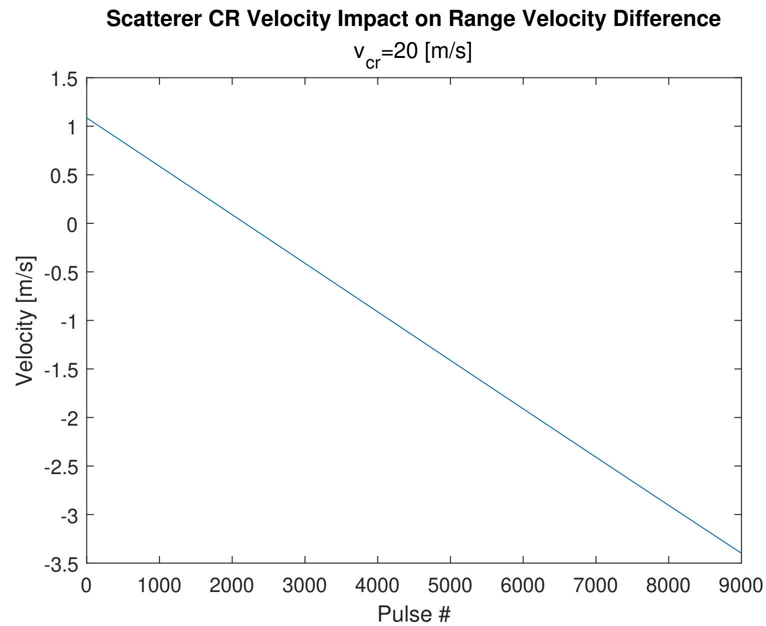

(a)

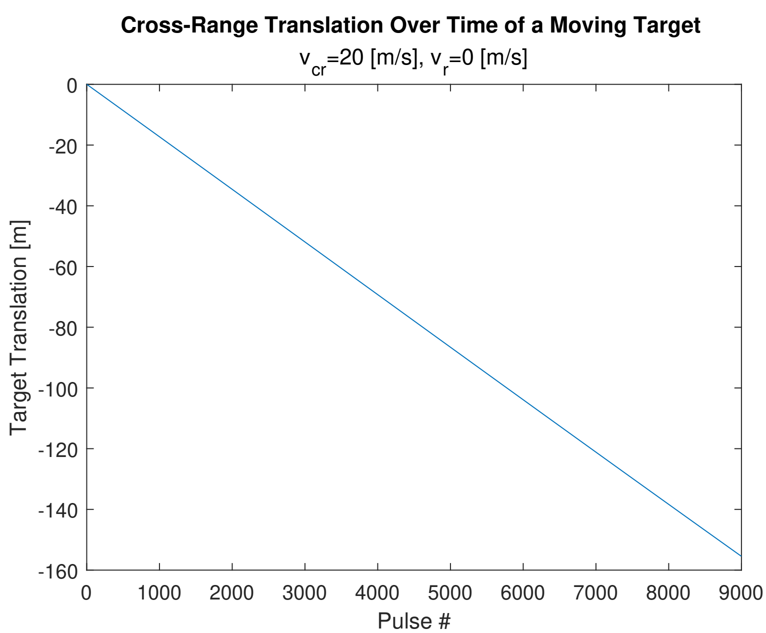

(b)

Figure 3.7: (a) The difference in range velocity between the moving scatterer and a stationary scatterer at the starting position. (b) The expected target displacement due to the range velocity difference in (a) as a function of pulse.

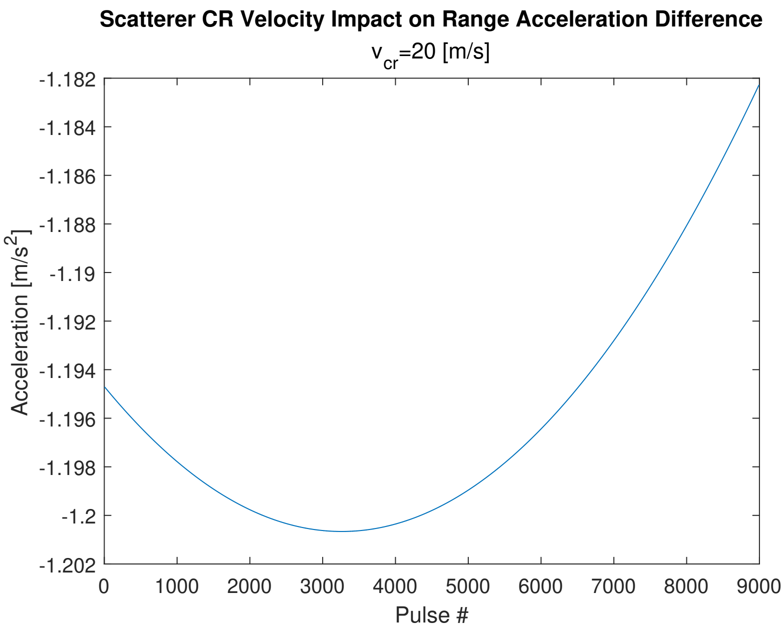

Figure 3.8: The impact of a cross-range velocity on range acceleration as the aspect angle changes.

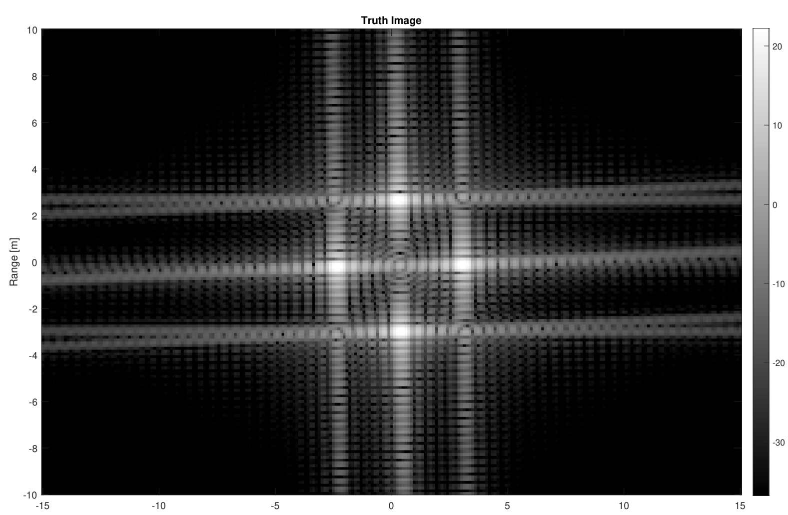

Figure 3.9: Synthetic target ISAR backprojection truth image.

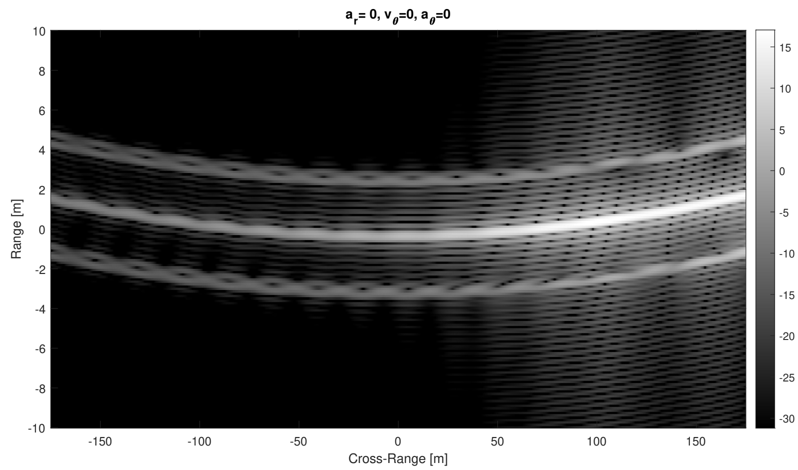

Figure 3.10: Synthetic target backprojection image assuming a stationary target.

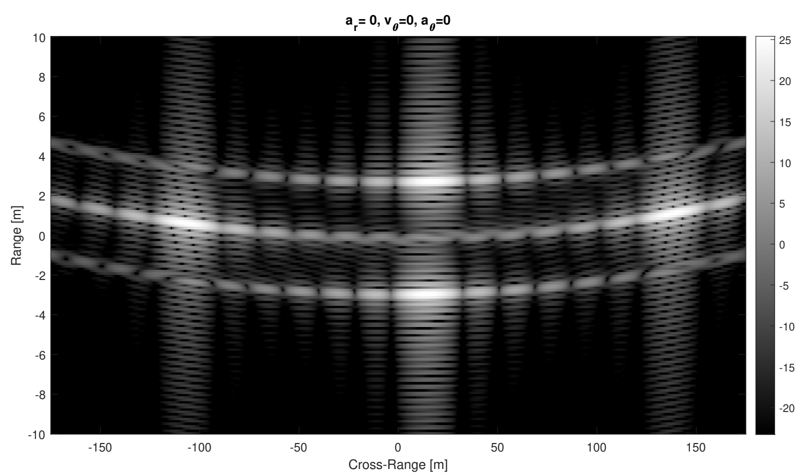

Figure 3.11: Synthetic target ISAR backprojection image accounting for truth translational motion with no rotational motion compensation. Observe the cross-range width of the target.

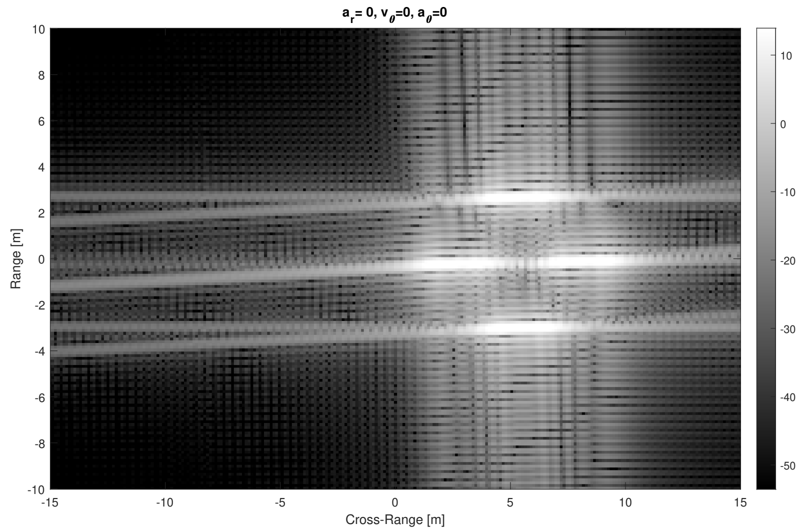

Figure 3.12: Synthetic target ISAR backprojection image accounting for truth rotational motion with no translational motion compensation. Compare the cross-range width of the target with that in the image with no rotational motion compensation (Fig. 3.11)

Image Smear Caused by Translational Motion

The amount of smear expected from cross-range velocity, v_{CR}, is given by

$$\mu_{CR} = 2v_{CR}T_{SAR}, \tag{3.8}$$

where T_{SAR} is the time duration of the synthetic aperture used to make the image. The smear expected from a range acceleration, a_r, is given by

$$\mu_{CR} = \frac{a_R T_{SAR} R_0}{v_p}. \tag{3.9}$$

The amount of smear that would be caused by the simulated target with a 20 [m/s] cross-range velocity according to (3.8) is 150 [m]. Figure. 3.7 shows the impact that a constant cross-range velocity has on the range velocity as the aspect angle changes. The expected target displacement due to the velocity difference

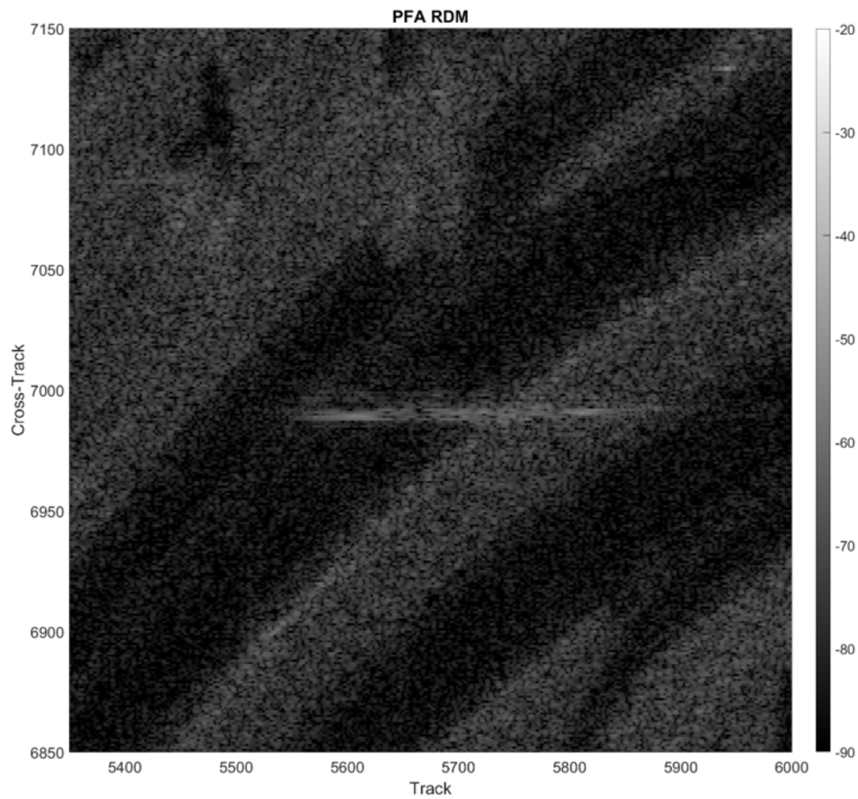

Figure 3.13: Smeared moving target in GOTCHA data PFA image.

from the beginning to the end of the aperture time is 155.4 [m]. This displacement is effectively measuring the width of the smear caused by range acceleration. The mean range acceleration of the data shown in Figure 3.8 is -1.196 [m/s] which will cause a smear of 155.25 [m].

The difference between the expected smear caused by v_{CR} and the smear caused by the range acceleration that manifests from it is within 4%. While cross-range velocity contributes to target smear, a target's cross-range velocity may manifest as a range acceleration that causes approximately the same amount of smearing in the image. Without prior knowledge of the vehicle's motion, it is unclear which parameter is contributing to the image smear.

v_{CR} smear	150 [m]
a_r smear	155.25 [m]
δv_r displacement	155.4 [m]

Table 3.2: The expected smear due to a cross-range velocity compared to the expected smear and displacement due to its impact on other parameters.

Image Smear Caused by Rotational Motion

Rotation causes the target energy to stretch in both the positive and negative cross-range directions (Fig. 3.11). The stretching is a consequence of the rotation, which contributes a positive Doppler velocity to one side of the object and a negative Doppler velocity to the other. The stretch factor is the inverse of the scale factor presented in Chapter 5 (eq. 5.9).

The simulated rigid body is given a large rotation rate of 90 [deg/s]. When you observe the differential range between the second scatterer and the center of the rigid body, the range profile of the second scatterer is a sinusoid with a frequency of 0.25 Hz (Fig. 3.14). The consequence of this is that every order of derivative will be sinusoidal. The range velocity and range acceleration are consequently sinusoidal, as observed in Figures 3.15 and 3.16.

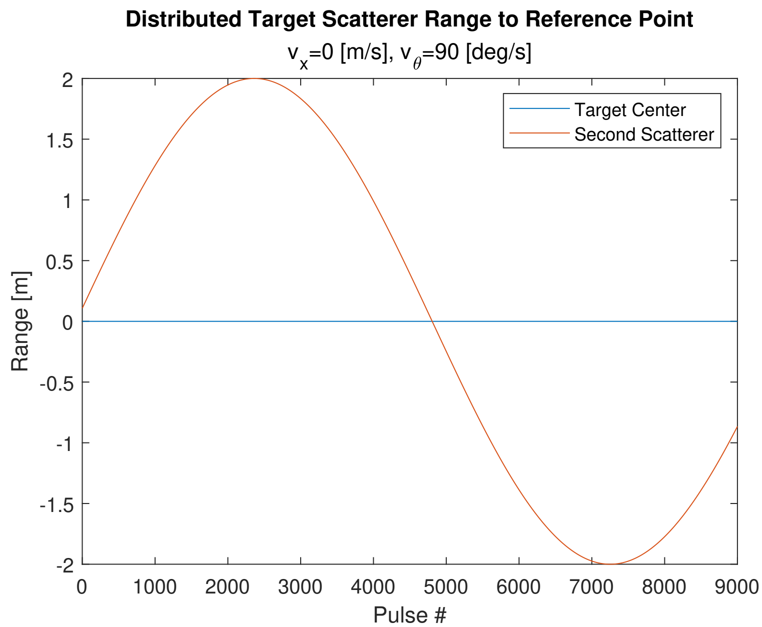

Figure 3.14: Range Migration of a scatterer rotating around some reference point.

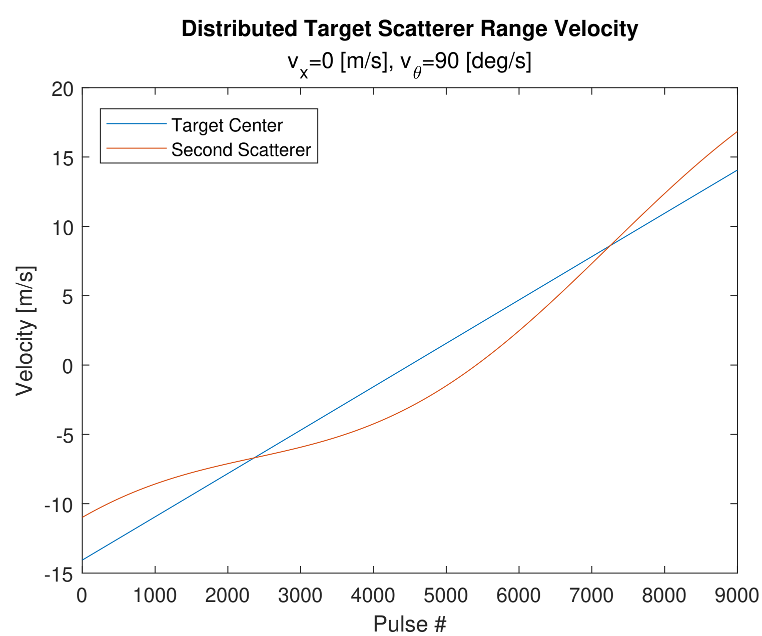

Figure 3.15: Range velocity of a scatterer rotating around some reference point.

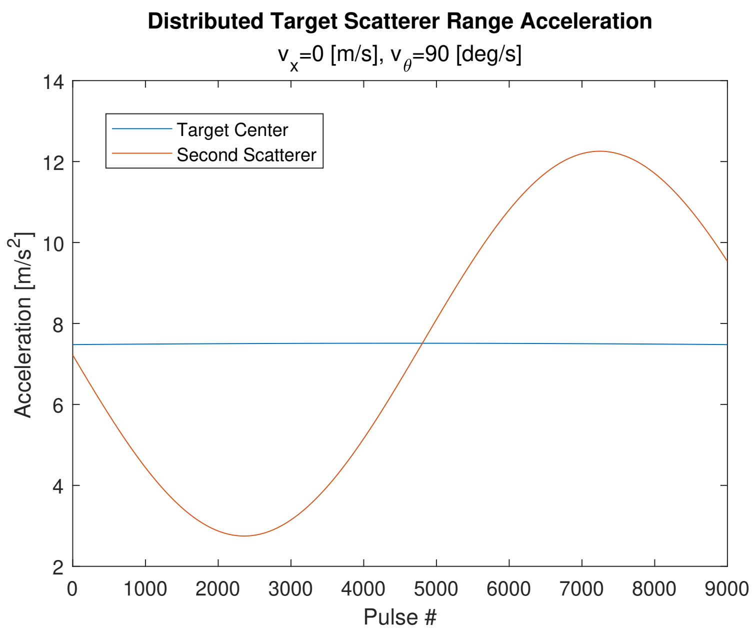

Figure 3.16: Range acceleration of a scatterer rotating around some reference point.

Chapter 4

Image Sharpness Based Autofocus for Non-Cooperative Targets

The proposed autofocus technique estimates target motion parameters through a parameter search using an image sharpness metric as the optimization criterion. After a target has been detected and approximate estimates of Doppler velocity and position have been obtained, a search is conducted for range acceleration followed by a search for rotation rate. Range acceleration is first used to approximate the target's mean range profile, followed by a rotation-rate search to account for range migration of distributed scatterers on the target relative to that mean profile. The target is assumed to be a ground moving target, with acceleration and rotation occurring in the imaging plane.

The proposed method assumes that, over a short time interval, the motion profile of a distributed object can be modeled by a starting range velocity, constant range acceleration, and constant rotation rate. All autofocus results presented in this thesis are based on processing intervals shorter than 0.5 seconds.

The focusing process is as follows:

1. Obtain approximate estimates of the target position and range velocity. The estimated position defines the initial center of the image grid. The estimated range velocity is held constant during the range acceleration search

2. Form a range v. cross-range image grid of pixels.

3. Search over the range acceleration hypothesis while holding the average range velocity constant. The hypothesis that produces the sharpest image is chosen.

4. Search over rotation rate hypotheses using the estimated range acceleration. The cross-range extent and resolution must be scaled before forming the image for a given hypothesis. The hypothesis that produces the sharpest image is chosen.

The precise method for coherently combining focused images remains an area for further investigation. The first image will follow the outlined procedure. Given a focused image, the pixel grid for the second image should begin at the position at which the grid for the first ended. The size and resolution of the second image should also equal those of the first. Scaling the second image's cross-range dimension will prevent it from coherently adding to the first; however, the measured sharpness of the second image will still be skewed by the rotation hypothesis. While the method remains unknown, there must be some compensation for the skewed sharpness.

4.1 Image Sharpness Metric

A commonly used image quality metric in the ISAR literature is image entropy [6]. However, the analysis performed in this work showed that image sharpness is a more robust metric for determining when a target is optimally focused. The metrics are compared later in Chapter 5. Regardless of the chosen metric, successful autofocus for a moving target requires a sufficiently high signal-to-clutter ratio (SCR) within the image.

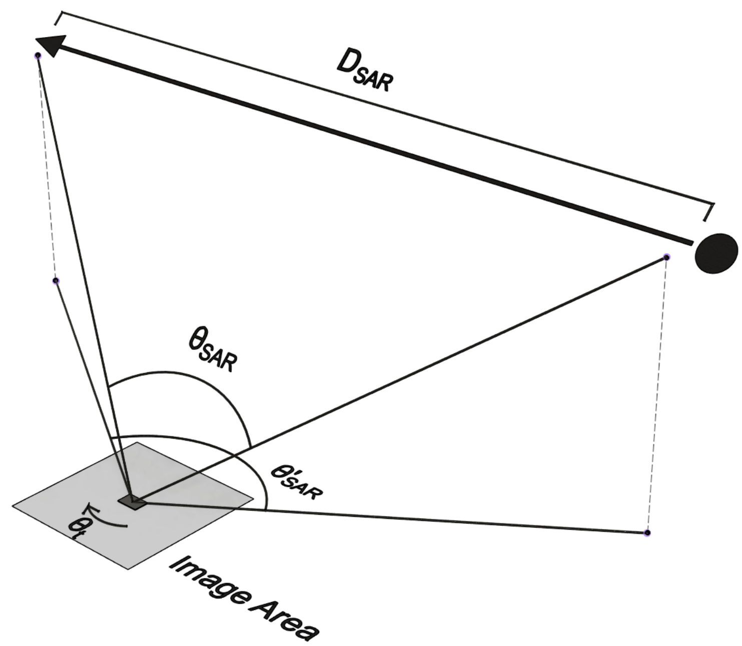

Figure 4.1: 3-D SAR Geometry showing the projected aperture.

Muller and Buffington showed that a variety of image sharpness metrics reach their maximum when the image is optimally focused [35]. Following the approach of Fienup, this work employs their first sharpness metric, defined as the square of the image intensity given by [33]

$$S_1 = \sum_{x=1}^{X} \sum_{y=1}^{Y} |g(x,y)|^4, \tag{4.1}$$

where S_1 is the measured sharpness of the image, $g(x, y)$ is the complex-valued image, and x and y denote the image indices.

4.2 Two Part Parameter Search

The autofocus algorithm requires an initial estimate of the target's position and range-velocity. These estimates may be obtained from a GMTI algorithm, phase-error detection [33], or CFAR detection following single-channel clutter cancellation [36]. Regardless of the detection method, only an approximate position and range velocity are required to initialize the autofocus process.

4.2.1 Translational Motion Compensation

The target range acceleration search occurs in the image plane, which lies on Earth's surface. Expressing the search in Cartesian coordinates yields parameters that more naturally describe ground-vehicle motion.

An exhaustive search over Cartesian velocity hypotheses reveals that image sharpness is largely insensitive to the hypothesized range velocity over a short aperture time (see Section 5.3). Recall from Section 3.2 that a target's range velocity causes a displacement in SAR images. Since range velocity primarily translates the target within the image, it need not be included in the parameter search once the target has been centered in the image under test. Adjusting the hypothesized range velocity when the target is already within the image will cause an unwanted image shift. Given this result, a velocity search should be limited to the cross-range dimension.

Further analysis shows that the cross-range velocity manifests a range acceleration (3.3). The range direction changes as the antenna completes its aperture (5.10), causing the once pure cross-range velocity to have a changing range component. This change in range velocity from the beginning to the end of the coherent processing interval (CPI) causes an estimated displacement that is approximately equal to the estimated smear width due to the cross-range velocity (table 3.2). This limits the TMC to the range dimension. Range acceleration is the only translational motion parameter that needs to be searched.

Translational motion compensation is accomplished by matching the range profile. The true translational motion of the vehicle on the image plane is characterized by a changing 2-D vector, but the radar only observes the 1-dimensional range migration. The reduced dimensionality reduces the search space; however, some information about the target's complex motion is lost. Consequently, there is ambiguity in the combination of ground-motion parameters that produced the observed range migration.

Once the target is detected, the measured range-velocity and position of the target serve as the initial parameters for the focusing algorithm. This can be in the form of an initial position and initial range velocity, or it can be based on the location that the blurred target appears in the image.

Once the target location has been estimated, an image grid is constructed large enough to contain the smeared target in both range and cross-range. The image size must be constrained to allow only a few meters between the image edges and the smeared target. Once the TMC has been applied to the target, it can be trimmed down further if necessary. The image should be as small as possible to reduce the likelihood that clutter will significantly bias the sharpness measurement.

The image resolution must be over-sampled. If the pixel spacing equals the nominal image resolution, the peak response of a scatterer may fall between adjacent pixels, causing the measured image sharpness to depend on pixel alignment rather than image focus. In this case, the measured sharpness does not accurately reflect image focus. In this work, the image resolution has been halved (Fig. 4.2).

The image grid will move based on the starting range velocity and range acceleration hypothesized. First, project the line of sight vector from the antenna to the target onto the image plane. Because the line of sight vector is changing throughout the aperture time, the vector is from the middle pulse of the processing interval is

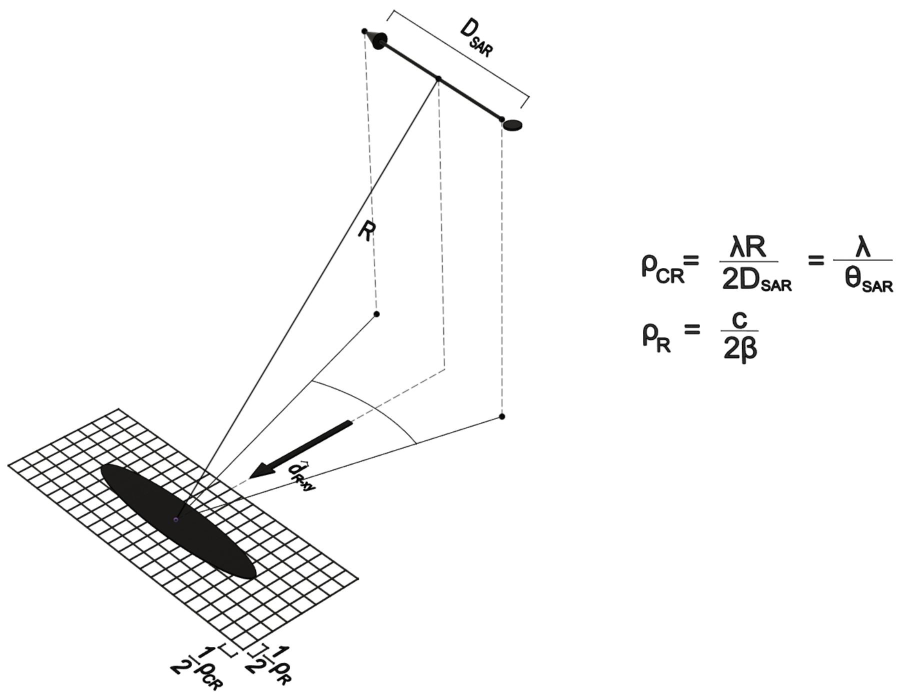

Figure 4.2: ISAR backprojection image grid orientation and size relative to target energy spread in the image.

chosen. The projected line of sight unit vector is denoted by $\hat{\mathbf{d}}_{R-xy}\left(\frac{M_{CPI}}{2}\right)$. The grid will shift towards or away from the radar based on the hypothesized acceleration.

The acceleration can be searched exhaustively within predefined bounds or via a gradient search. The search limits used for the observed vehicle were between plus and minus 5 [m/s^2] with a spacing of 0.2 [m/s^2]. The gradient search will be more efficient but may not find the global maximum when the image contains clutter.

Let $\mathbf{c}_1$ be the center of the imaging grid in Cartesian coordinates on the first pulse. The image center is translated on each pulse according to the hypothesized range motion. The pulse-by-pulse $3 \times M$ image center will be defined as

$$\mathbf{c}_g(m) = \mathbf{c}_1 + \left(\left(v_r - a_r\frac{M}{2}\right)(m-1) + \frac{1}{2}a_r(m-1)^2\right)\hat{\mathbf{d}}_{R-xy}\left(\frac{M_{cpi}}{2}\right) \quad (4.2)$$

where v_r is the average velocity (v_r fixes the position of the target in cross-range during the focusing process), a_r is the hypothesized range acceleration, and M_{cpi} is the number of pulses in the processing interval. If the pulse repetition interval (PRI) is known, then substitute m for time in seconds and M for the aperture time. If it is unknown, then m is the pulse index and M is the number of pulses. The velocity and acceleration are then measured by pulses rather than time.

Before estimating the target rotation, the target should be centered within the image. The rotational motion model is defined about the range profile of the center pixel; therefore, any translational offset may harm the rotational motion compensation. This can be accomplished after TMC by finding the range and cross-range offset in the image. The target offset is estimated using the image center of mass. A threshold should be applied to reduce the impact of clutter. Thresholding at the 99.7th percentile of pixel magnitude has proven successful. This requires the image to have a sufficiently high SCR after TMC.

The range offset is projected onto the range direction, and the image grid's starting position is updated accordingly. The starting range position of the image will now be

$$\mathbf{c}_g(m) = \mathbf{c}_1 + \left(\left(v_r - a_r\frac{M}{2}\right)(m-1) + \frac{1}{2}(a_r(m-1)^2 + R_{xy-off}\right)\hat{\mathbf{d}}_{R-xy}\left(\frac{M_{cpi}}{2}\right), \tag{4.3}$$

where R_{xy-off} is the evaluated offset in range.

The cross-range offset may be compensated either by translating the image grid or by adjusting the average radial velocity. If the grid's starting position depends on where the target appears in the image, then apply a shift in the cross-range direction to the grid. If initial parameters rely on an initial position and range velocity, then adjust the range velocity. Rearranging eq. 3.7 yields the required radial velocity correction, given by

$$v_r = -\frac{C_{xy-off}v_p}{R_0}, \tag{4.4}$$

where C_{xy-off} is the cross-range offset. The range velocity here is projected onto the ground plane before adding it to the range velocity used to calculate the target position on each pulse in eq. 4.3. The projected velocity is given by

$$v_{r-xy} = \frac{v_r}{\cos\theta_{el}}, \tag{4.5}$$

where θ_{el} is the antenna elevation angle.

When coherently combining consecutive sub-CPIs, continuity between adjacent images is preserved by propagating the target state from the end of one CPI to the beginning of the next. Consequently, the starting radial velocity is used instead of the average radial velocity. The image grid center is then defined as

$$\mathbf{c}_g(m) = \mathbf{c}_1 + \left(v_r(m-1) + \frac{1}{2}(a_r(m-1)^2\right)\hat{\mathbf{d}}_{R-xy}\left(\frac{M_{cpi}}{2}\right). \tag{4.6}$$

$\mathbf{c}_g(m)$ defines a path on the ground with the same range profile as the target. Due to the ambiguities discussed in 5.3, the true ground path could be any combination of parameters that create the same range profile. The translational motion parameters describe the observed range migration rather than the true ground trajectory. After the target translational motion has been compensated, the next step estimates the rotational motion independently.

4.2.2 Rotational Motion Compensation

Translational motion compensation accounts for the target's range migration but does not account for target rotation during the CPI. The aperture with respect to the target differs from that assumed by conventional SAR image formation, resulting in a stretched target. Therefore, rotational motion compensation (RMC) is required after TMC. The hypothesized rotations attempt to account for the range migration of the distributed scatterers that make up the rigid body.

Before testing a rotation hypothesis, the cross-range extent and pixel spacing must be scaled, because each hypothesis changes the effective synthetic aperture. Without this scaling, image sharpness varies with geometry rather than with image focus alone, rendering comparisons between hypotheses invalid.

The projected angular aperture on the imaging plane is first determined. Then the cross-range pixel width is scaled by the ratio of the original aperture to the new aperture (Fig. 4.1). The scale factor is given by

$$\kappa_{CR} = \frac{\theta'_{SAR}}{\theta'_{SAR} - \theta_t}, \tag{4.7}$$

where θ'_{SAR} is the angle of the aperture projected onto the image plane and θ_t is the amount of rotation experienced‘ by the target. The two angles must retain their sign indicating positive or negative rotation. This scale factor experiences a singularity at $\theta'_{SAR} = \theta_t$. When $\theta'_{SAR} = \theta_t$, the effective synthetic aperture becomes zero, causing the cross-range resolution to become undefined.

Because the target motion is assumed to lie in the imaging plane, the radar LOS vectors are projected onto that plane before computing the effective aperture. The projected aperture is the angle between the first LOS vector, $\mathbf{r}'_1$, and the last LOS vector, $\mathbf{r}'_M$, in the CPI. The projected vectors are given by

$$\begin{aligned} \mathbf{r}'_1 &= \langle \mathbf{r}_1, \hat{\mathbf{x}} \rangle \hat{\mathbf{x}} + \langle \mathbf{r}_1, \hat{\mathbf{y}} \rangle \hat{\mathbf{y}}, \\ \mathbf{r}'_M &= \langle \mathbf{r}_M, \hat{\mathbf{x}} \rangle \hat{\mathbf{x}} + \langle \mathbf{r}_M, \hat{\mathbf{y}} \rangle \hat{\mathbf{y}}, \end{aligned} \tag{4.8}$$

where $\mathbf{r}_M$ is the radar LOS vector to the target on pulse M , which is the last pulse in the CPI, and $\mathbf{r}_1$ is the first LOS vector in the CPI. $\hat{\mathbf{x}}$ and $\hat{\mathbf{y}}$ are the original x and y directions that define the image. They can be three-dimensional vectors in ECEF that define East and North or any other orthogonal directions that define the image plane. The angle between these two projected LOS vectors is

$$\theta'_{SAR} = \arccos\left(\frac{\langle \mathbf{r}'_1, \mathbf{r}'_M \rangle}{||\mathbf{r}'_1||\ ||\mathbf{r}'_M||} \right). \tag{4.9}$$

The target's rotation, θ_t, is defined by the CPI duration and the hypothesized rotation rate defined by

$$\theta_t = v_\theta M, \tag{4.10}$$

where v_θ is the hypothesized rotation rate and M is either the number of pulses or the time duration of the processing interval.

The scale factor (4.7) is applied to the cross-range extent and resolution of the image grid. The scaled cross-range extent is

$$L'_{CR} = \kappa_{CR} L_{CR}, \tag{4.11}$$

where L_{CR} is the original cross-range extent of the image in meters. The new cross-range resolution is given by

$$\rho'_{CR} = \kappa_{CR} \rho_{CR}, \tag{4.12}$$

where ρ_{CR} is the original cross-range resolution of the image grid.

For each rotation rate, the image grid will rotate about the center pixel. The amount of rotation experienced by the image grid, $\theta_G(m)$, from pulse-to-pulse is defined by

$$\theta_G(m) = v_\theta m + \theta_{CR}, \tag{4.13}$$

where m is either time or pulse index, and θ_{CR} is the rotation that is needed to align the grid along the projected range and cross-range directions.

Let $\mathbf{G}_x$ and $\mathbf{G}_y$ denote matrices containing the cross-range and range coordinates of every pixel relative to the image center, respectively. Both matrices are centered at zero and together define the image grid prior to rotation. The range direction is $\hat{\mathbf{d}}_{R-xy}\left(\frac{M_{cpi}}{2}\right)$, and the cross-range direction is $\hat{\mathbf{d}}_{R-xy}\left(\frac{M_{cpi}}{2}\right)$ rotated by $90°$.

The scaling is applied to $\mathbf{G}_x$ after TMC and before the image has been formed.

The new scaled cross-range positions are given by

$$\mathbf{G}_{x\kappa} = \mathbf{G}_x \kappa_{CR}. \tag{4.14}$$

This scaled grid accounts for both the cross-range extent scaling and the resolution scaling.

The pixel grid is rotated pulse-by-pulse and used to calculate the differential range to each pixel in the backprojection image formation process. The new pixel positions with respect to their original $\hat{\mathbf{x}}$ and $\hat{\mathbf{y}}$ vectors will now be

$$\begin{aligned}\mathbf{G}'_x(m) &= \mathbf{G}_{x\kappa}\cos(\theta_G(m)) - \mathbf{G}_y \sin(\theta_G(m)), \text{ and}\\ \mathbf{G}'_y(m) &= \mathbf{G}_{x\kappa}\sin(\theta_G(m)) + \mathbf{G}_y \cos(\theta_G(m)).\end{aligned} \tag{4.15}$$

The rotated image grid is then mapped into the three-dimensional imaging coordinate system using the direction vectors $\hat{\mathbf{x}}$ and $\hat{\mathbf{y}}$. The Cartesian space in which the image grid lies is defined by 3 matrices of the same size as $\mathbf{G}_x$ and $\mathbf{G}_y$. The pixel positions that are used to calculate the differential range for the phase correction in eq. 2.17 are given by

$$\begin{aligned}\mathbf{X}(m) &= \mathbf{G}'_x(m)\hat{\mathbf{x}}(1) + \mathbf{G}'_y(m)\hat{\mathbf{y}}(1) + \mathbf{c}_g(m,1),\\ \mathbf{Y}(m) &= \mathbf{G}'_x(m)\hat{\mathbf{x}}(2) + \mathbf{G}'_y(m)\hat{\mathbf{y}}(2) + \mathbf{c}_g(m,2),\\ \mathbf{Z}(m) &= \mathbf{G}'_x(m)\hat{\mathbf{x}}(3) + \mathbf{G}'_y(m)\hat{\mathbf{y}}(3) + \mathbf{c}_g(m,3).\end{aligned} \tag{4.16}$$

This process is repeated for each rotation rate hypothesis.

Because the sharpness surface is mirrored about the singularity (See Fig. 5.20), searching rotation rates on both sides of the singularity is redundant. It is recommended to use the singularity as one of the bounds of the rotation rate search.

To add a second image coherently, the new pixel positions must start where the previous image ended. Maintaining consistent pixel positions is required for image registration between successive sub-CPI's. Let θ_{G-1} represent the angular position of the pixel grid on the last pulse of the first image. The grid rotation angle for the second image will be

$$\theta_G(m) = v_\theta m + \theta_{G-1}. \tag{4.17}$$

No new scaling should be applied to the imaging grid. The cross-range extent and pixel spacing should be preserved in the new image; however, the measured sharpness must still be compensated for, but the method for doing so requires further investigation.

Chapter 5

Analysis and Results

5.1 Datasets

The analysis presented in this chapter uses two datasets and two simulated distributed targets. The first dataset is single-channel GOTCHA data collected over Dayton, Ohio. The synthetic targets were prepared for injection into this GOTCHA dataset. The second dataset consists of satellite SAR data collected in April 2026, purchased by the Advanced Radar Research Center (ARRC). The ARRC data contains several instrumented movers to aid in testing the autofocus algorithm.

5.1.1 Synthetic Moving Target

The synthetic distributed target provides a baseline for evaluating the proposed autofocus technique. The target's known motion profile is used to generate a reference image, which is then compared with an autofocused image formed using the technique described in chapter 4. The target begins with constant velocity for the first 3,000 pulses, accelerates, then starts turning on pulse 6,000. It completes the turn on pulse 21,000, accelerates for another 3,000 pulses, and then finishes the final 6,000 pulses with a constant velocity (Figs. 5.3, 5.1).

The simulated mover was generated for injection into the GOTCHA data set.

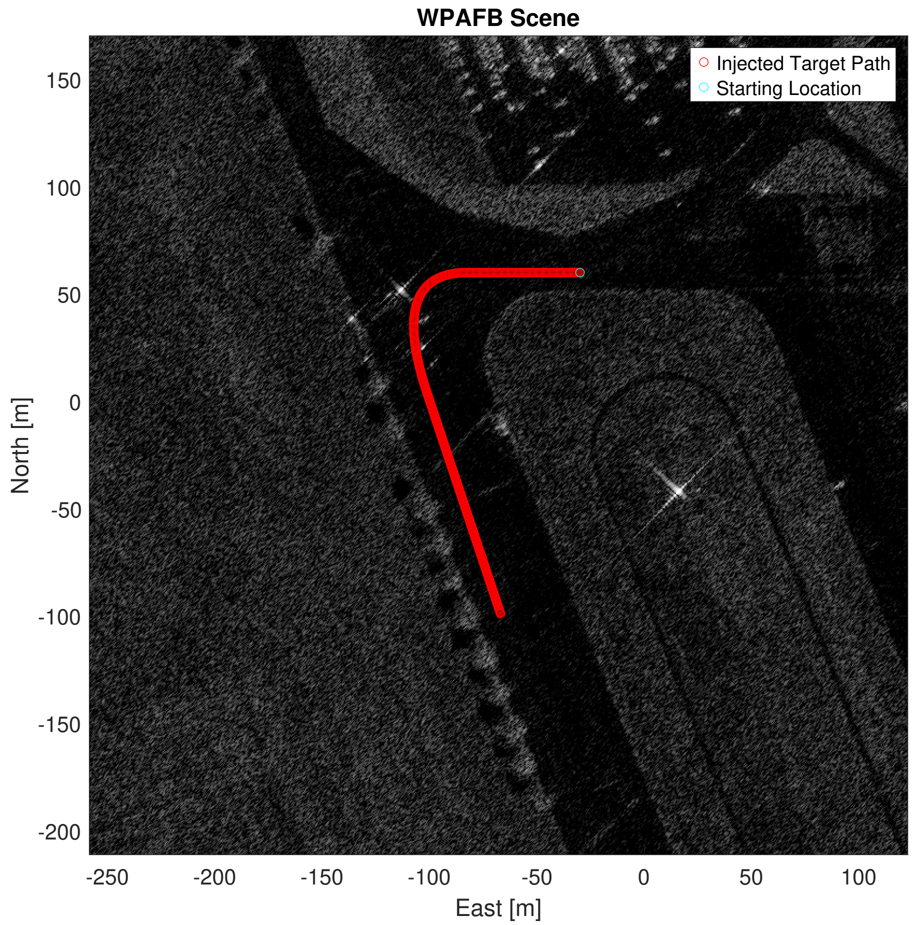

Figure 5.1: Synthetic distributed target path.

The simulated data can be tested in the absence of clutter or noise, allowing the algorithm to be evaluated under favorable conditions. Figure 5.4 shows the fully focused image formed using the target's known motion profile.

5.2 Image Quality Metric Comparison

Automated image analysis requires a metric to determine which autofocus hypothesis produces the highest-quality image. Some commonly used metrics include

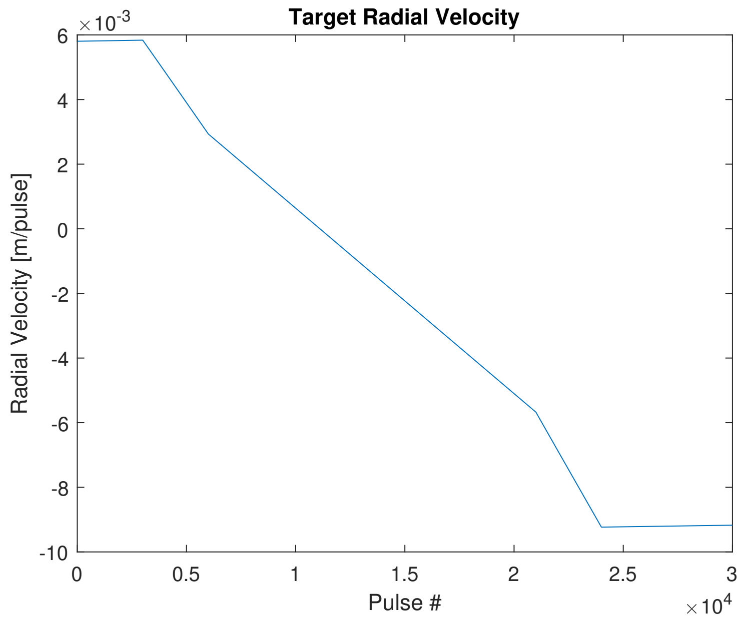

Figure 5.2: Synthetic distributed target radial velocity.

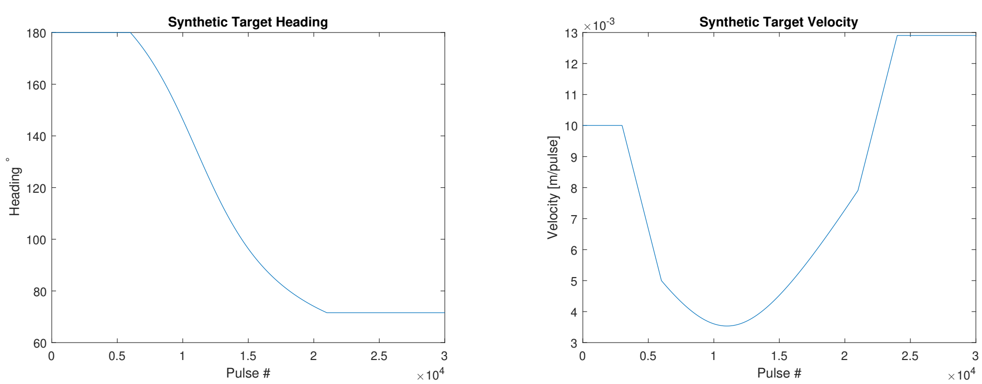

(a) Target Heading in degrees.

(b) Target velocity in meters/pulse

Figure 5.3: Synthetic distributed target motion parameters

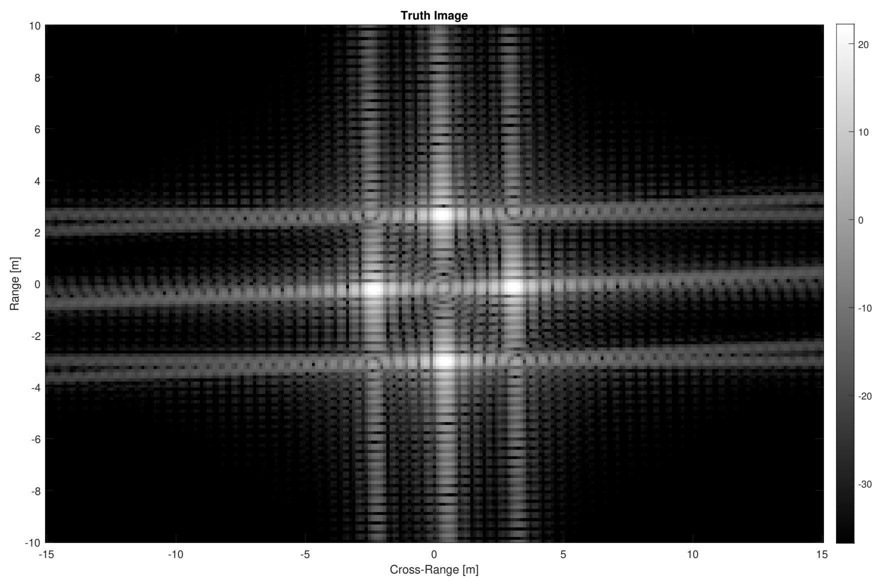

Figure 5.4: Synthetic distributed target focused using the known truth motion parameters over 500 pulses with no clutter.

image sharpness, variance, and entropy. Image entropy is commonly used in the SAR literature to evaluate image focus[6, 8]. Image entropy, ε, is defined as [26]

$$\varepsilon = \sum_{x=1}^{X} \sum_{y=1}^{Y} \frac{|g(x,y)|^2}{S} \ln \frac{S}{|g(x,y)|^2} \tag{5.1}$$

where

$$S = \sum_{x=1}^{X} \sum_{y=1}^{Y} |g(x,y)|^2, \tag{5.2}$$

and where $g(x, y)$ is the complex image and x and y denote the image indices.

This work uses the first sharpness metric proposed by Muller and Buffington [35], which Fienup later employed for detecting moving targets [33]. The metric is the sum of the squared pixel intensity for all pixels in the image. Image sharpness is defined by

$$S_1 = \sum_{x=1}^{X} \sum_{y=1}^{Y} |g(x,y)|^4. \tag{5.3}$$

The two metrics were evaluated using both simulated and measured data to determine which was a more reliable criterion. Figure 5.5 shows the metric comparison during a rotation rate search for the simulated distributed target. The average target rotation for the CPI is marked in each plot. The sharpness metric yields a peak near the known rotation rate, whereas the entropy metric does not produce a corresponding minimum.

In a real scenario with the instrumented target that was operated by MiLa, the entropy metric produced two local minima, requiring an additional criterion to select the optimum parameter value (Fig. 5.6). Of these two minima, the lowest yields what appears to be a less focused image. According to these experimental results, the sharpness metric appears to be more robust than entropy. Thus, sharpness has been chosen as the image quality metric for this algorithm.

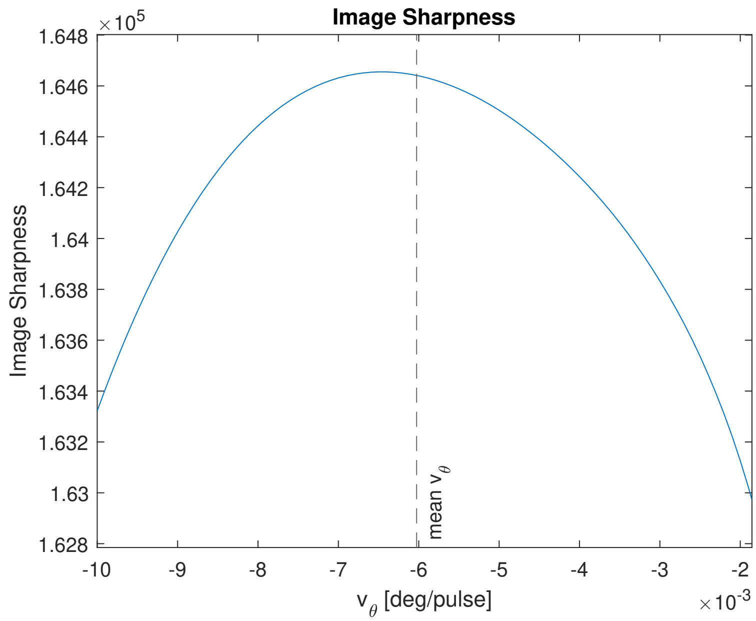

(a)

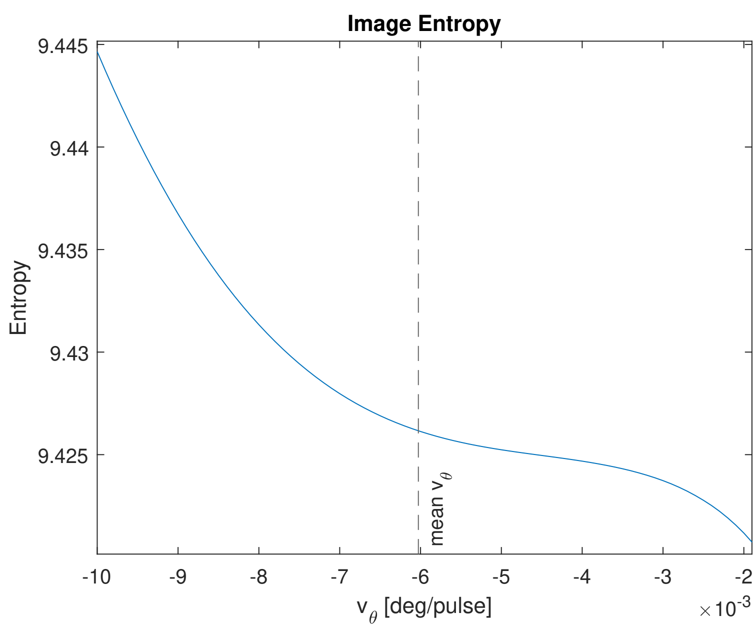

(b)

Figure 5.5: Comparison of image sharpness and entropy during the rotation-rate search for the synthetic distributed target. The vertical line indicates the true average rotation rate over the CPI.

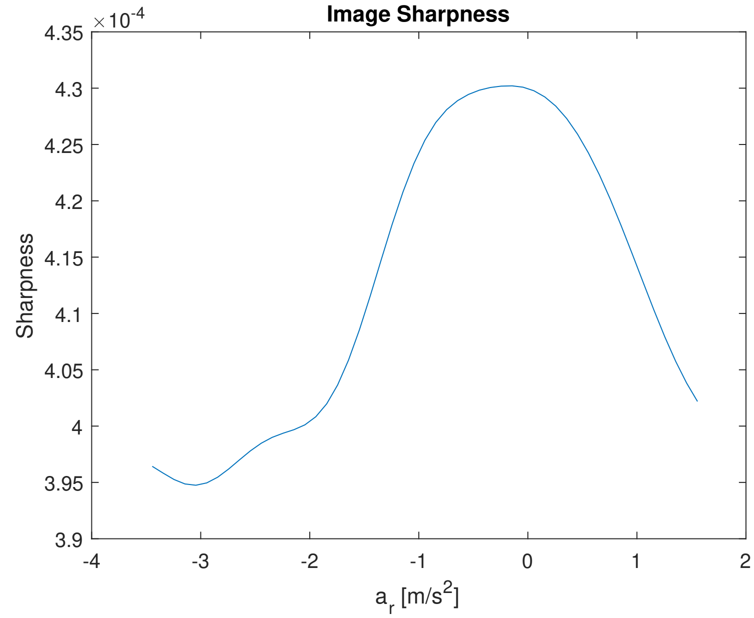

(a)

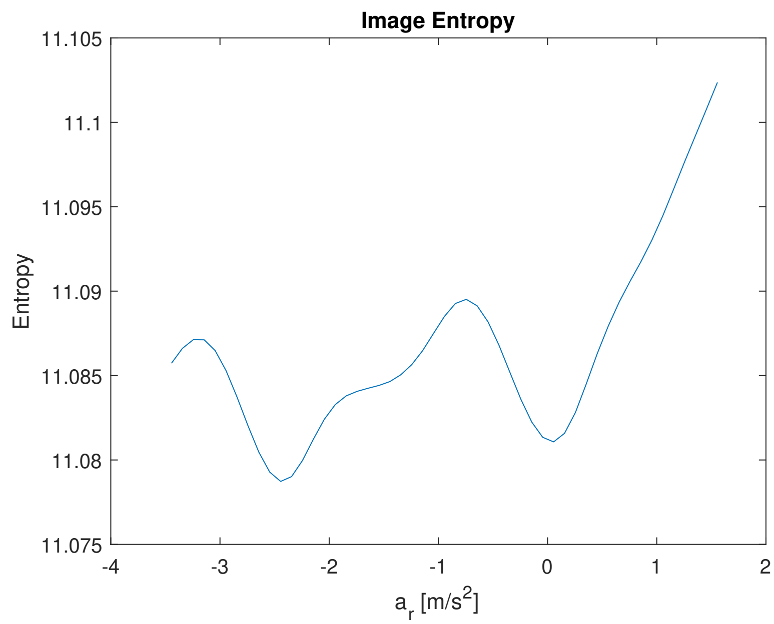

(b)

Figure 5.6: Comparison of image sharpness and entropy during the range acceleration search for the real distributed target.

5.3 Sharpness Metric Sensitivity to Motion Parameters

5.3.1 Translational Motion

Image sharpness is not equally affected by all motion parameters. To minimize computational complexity, parameters with minimal impact on image sharpness need not be included in the search. For example, a constant range velocity primarily causes image translation with minimal effect on image focus. A cross-range velocity or range acceleration, however, may cause substantial blurring [33].

The sensitivity of the sharpness metric to velocity was evaluated using a simulated point target. The simulated target is a point scatterer with zero velocity in the y-direction and a velocity of -6.6778×10^{-4} [m/pulse] in the x direction. Because the GOTCHA dataset does not include the pulse repetition frequency (PRF), velocity is expressed in meters per pulse.

Initial Parameter Analysis Using the Sharpness Metric

The velocity hypotheses are tested using the backprojection algorithm. For each hypothesis, the center of the imaging grid is moved on a pulse-by-pulse basis according to the velocity under test. The known starting location was used as the image grid center for these tests.

Because the tested velocities have varying magnitudes and directions, the range velocity will also vary. As discussed in Section 3.2, this changing radial velocity will cause the image to shift in the cross-range direction despite the starting position of the image being the target truth position. If the hypothesized range velocity is sufficiently large, the target may shift outside the image. To fairly compare images, this shift must be accounted for. The shift can be estimated using (3.7), and then compensated.

A simulated point target with constant velocity was first used to evaluate image sharpness as a function of x and y velocities. For each velocity hypothesis, the image center is shifted according to the estimated displacement. This ensures that the target energy remains centered in the image, so it can be consistently evaluated and compared.

The image sharpness measured for each velocity is shown in Figure 5.7. The center of the search grid corresponds to the target's true velocity. The observed ridge indicates that the image sharpness is significantly more sensitive to cross-range velocity than to range velocity. As long as the target energy remains centered in the image and the cross-range velocity is correct, the sharpness remains relatively constant regardless of the hypothesized range velocity. This result implies that range velocity can be excluded from the search. Image focus is primarily sensitive to the cross-range component of the target velocity.

The same experiment has been conducted using acceleration hypotheses in the x and y directions. As with the velocity test, there can be a small image-grid translation across different accelerations, because changing the acceleration hypothesis shifts the mean range velocity. To account for this, the image size needs to be sufficiently large to contain the target as the image moves. Another solution is to define the acceleration about the midpoint of the CPI by letting the time axis range from $-\frac{t}{2}$ to $\frac{t}{2}$. This keeps the mean velocity constant throughout the search and prevents image translation.

The acceleration search reveals a ridge similar to that observed in the velocity experiment except that the sensitivity is reversed: image sharpness is highly sensitive to radial acceleration but largely insensitive to cross-range acceleration (Fig. 5.8). If the correct range acceleration is being used, then the image sharpness re-

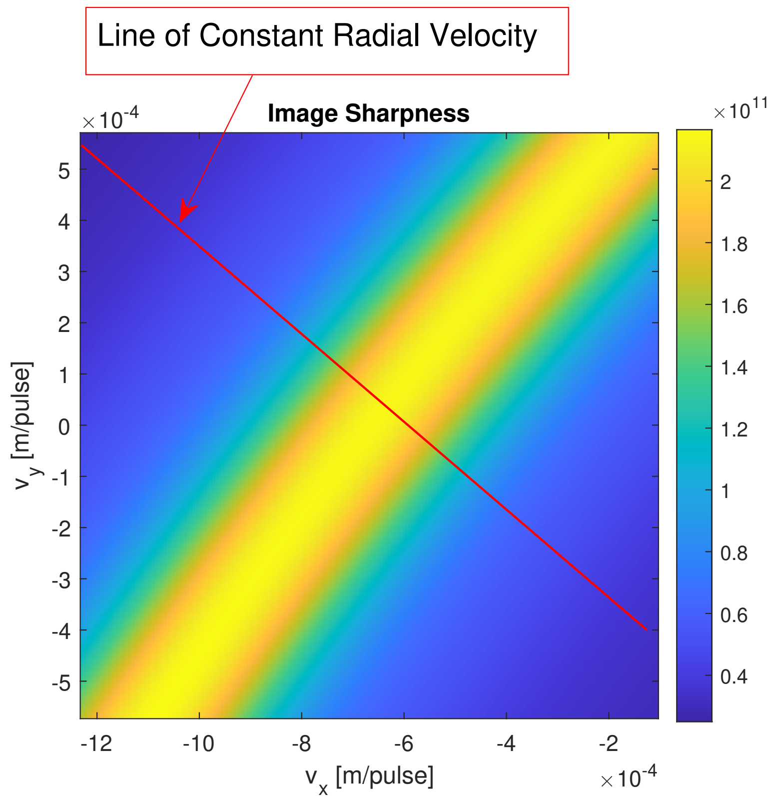

Figure 5.7: Sharpness surface for the two-dimensional velocity search. The ridge follows a curve of constant cross-range velocity, indicating that image sharpness is largely insensitive to radial velocity in this scenario.

mains relatively constant regardless of the cross-range acceleration hypothesis. This result implies that the search space can be reduced further to exclude cross-range acceleration from the parameter search.

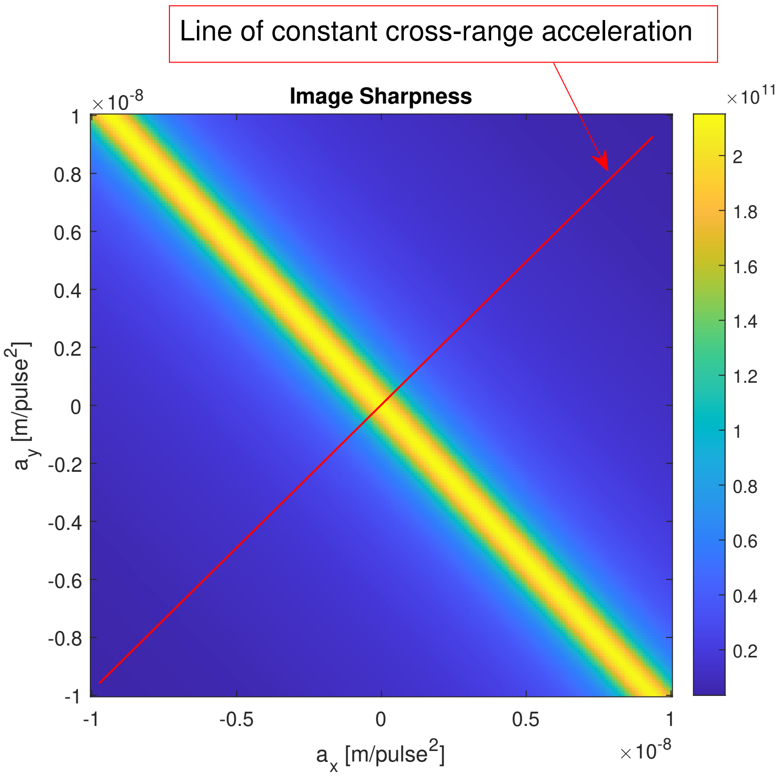

Figure 5.8: Sharpness surface for the two-dimensional acceleration search. The ridge aligns with the correct range acceleration while remaining largely insensitive to cross-range acceleration.

The final experiment on translational motion combines cross-range velocity and range acceleration hypotheses. This experiment was performed using a real target from the OU SAR collect. It was a GNSS-instrumented vehicle courtesy of the Mobility Intelligence Lab (MiLa) on the University of Oklahoma campus. The GNSS data provides an accurate enough estimate of the target position and range velocity to launch the autofocus algorithm; however, the position measurements are

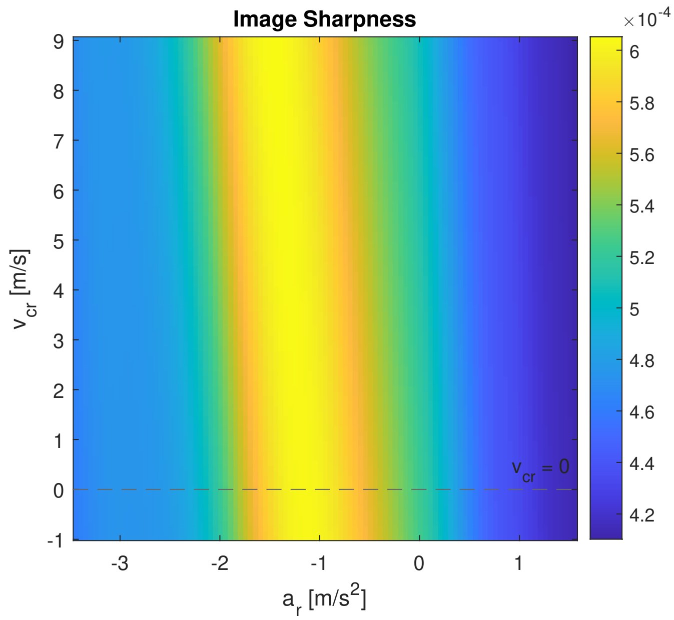

Figure 5.9: Image sharpness measured as a function of cross-range velocity and radial acceleration. The sharpness ridge indicates that the search dimensionality can be reduced to range acceleration.

not sufficiently precise to produce a fully focused reference image.

The parameter search was centered on the approximate cross-range velocity and radial acceleration derived from the GNSS measurements. The search yields another ridge, implying that a continuum of parameter combinations produces images with nearly identical sharpness (Fig. 5.9). The most significant observation is that the ridge intersects the line corresponding to zero cross-range velocity. Consequently, a solution exists which yields an approximately equally sharp image with no assumed cross-range velocity.

This result demonstrates that the search can be limited further to exclude cross-range velocity. This result is initially surprising, but the result can be explained by observing the changing geometry between the radar and the target. Consider a ground-moving target with a constant cross-range velocity and zero range velocity defined by the LOS vector of the middle pulse. The target velocity magnitude and direction on the ground can be approximated as a constant for a short interval. The airborne platform follows the trajectory described in Figure 3.1. As the antenna subtends some angle about the target, the velocity that is purely cross-range on the middle pulse has a radial component at the beginning and end of the aperture. This component changes as the perspective changes. As a result, a constant cross-range velocity manifests as a range acceleration.

To understand why cross-range velocity appears as range acceleration, consider the difference between the range velocity of a stationary scatterer and a moving scatterer. The stationary scatterer lies at the origin in the scenario from Chapter 3. The moving scatterer has the same initial position but is assigned a constant velocity in the positive x-direction of 20 $[m/s]$. The x direction is chosen because it is parallel to the cross-range direction at the origin at the midpoint of the CPI.

As the radar perspective changes throughout the aperture, the scatterer's radial velocity changes even though its ground velocity remains constant. Because the backprojection algorithm assumes a particular range profile, the changing range velocity induced by cross-range motion is not accounted for by the stationary-scene model. The mismatch causes the target energy to blur in the image.

Furthermore, the predicted cross-range smear from (3.8) is approximately equal to the cross-range smear estimated with the observed range acceleration (Table 3.2). The target motion can be viewed from the perspective of a cross-range velocity or range acceleration with similar outcomes

Decoupling the apparent range acceleration produced by cross-range motion from what was originally a pure radial acceleration is an area that requires further research [36]. A continuum of cross-range velocity and range acceleration combinations can produce the same observed range profile. Thus, the search for translational motion can be limited to radial acceleration. This reduction is justi-

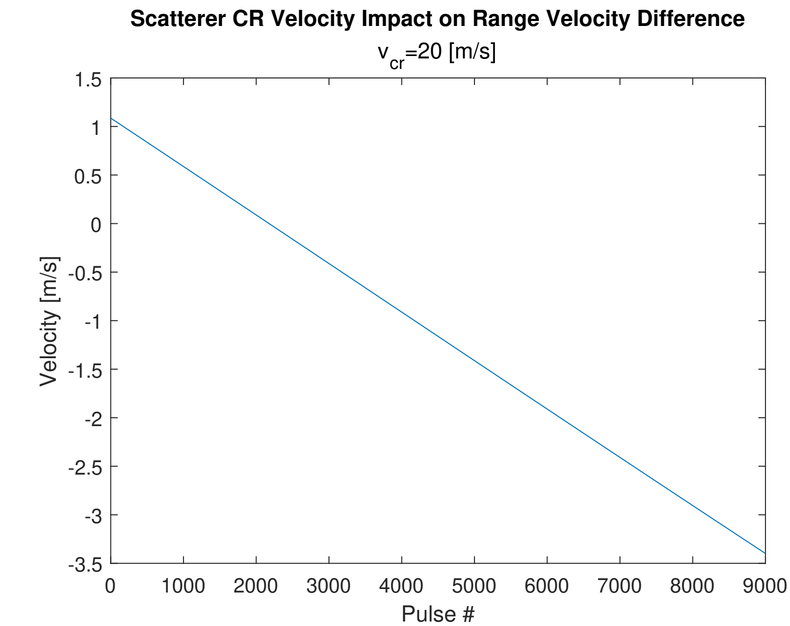

(a)

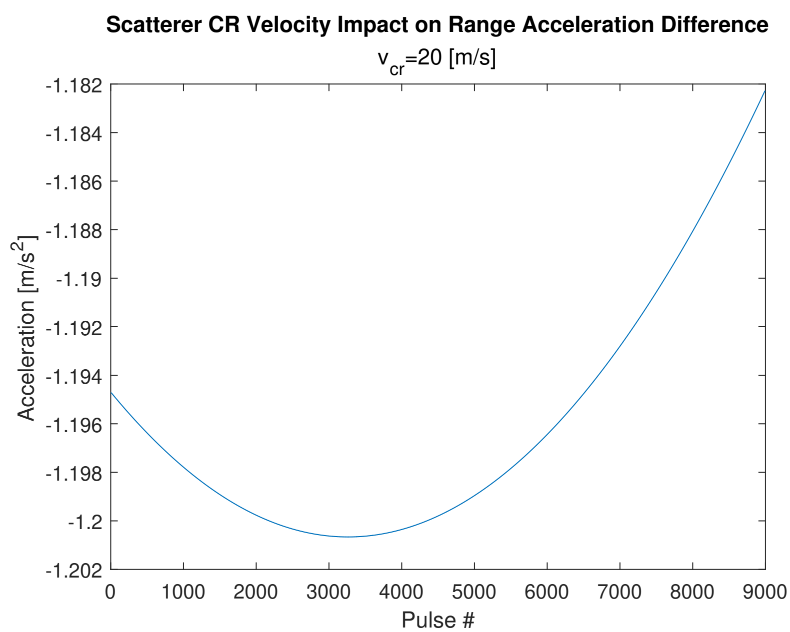

(b)

Figure 5.10: The difference in range velocity and acceleration between a stationary scatterer and a moving scatterer. (a) Difference in the range-velocity from pulse to pulse between a stationary scatterer and a scatterer with a 20 [m/s] cross-range velocity. (b) Difference in range acceleration for the same two scatterers.

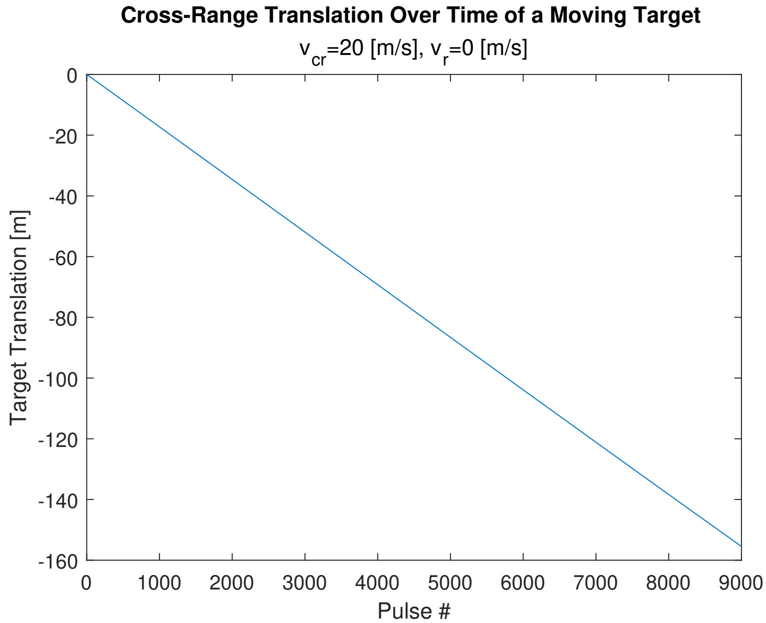

Figure 5.11: The amount of expected cross-range displacement due to the initial cross-range velocity according to eq. 3.7

fied because the observed range profile does not uniquely determine the cross-range velocity and radial acceleration components.

5.3.2 Rotational Motion

Target rotation causes the radial velocities of scatterers on opposite sides of the target to diverge. Even if the target's translational motion is perfectly compensated, target rotation causes the target energy to spread in both the positive and negative cross-range directions. From a resolution perspective, the target rotation changes the cross-range resolution that is achievable on the target (Fig. 5.13).

Consider a SAR scenario in which a vehicle is on a turntable. Consider several scatterers on the vehicle and examine their range migration. The target is rotating around its geometric center. The range migration of the target center serves as the nominal range profile for the distributed target. Consider two scatterers, A and B,

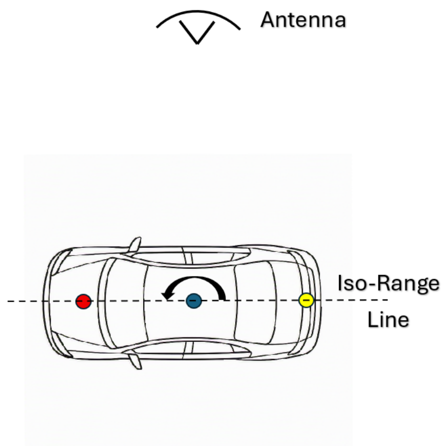

(a)

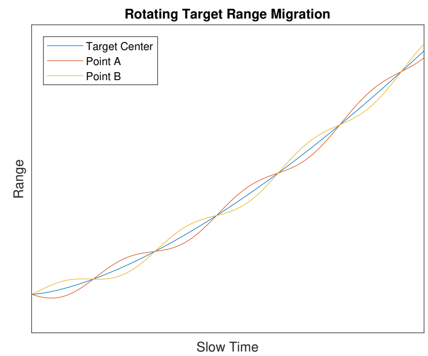

(b)

Figure 5.12: (a) Distributed target SAR scenario (b) Range profile of points within a distributed target rotating in place on a turntable.

that are initially aligned along the cross-range direction and equidistant from the target center. The scatterers have range profiles that diverges from the center of the target (Fig. 5.12).

After the translational motion of the target center has been compensated, each scatterer follows a slightly different range profile due to the target's rotation. This will manifest in the range profile as two sinusoids that are added to the range profile of the target center. The sinusoids' amplitudes are equivalent to the range displacement between them and the target center when the two points lie along the radar line of sight. The range profile of point (A) is given by

$$r_A(m) = r_t(m) + ||A - T_c|| \sin(\theta_A(m)), \tag{5.4}$$

where $r_t(m)$ is the pulse-dependent range of the target center point, $A - T_c$ is the distance between point A and the target center T_c, and $\theta_A(m)$ is the pulse-dependent angle that the scatterer makes with the cross-range dimension.

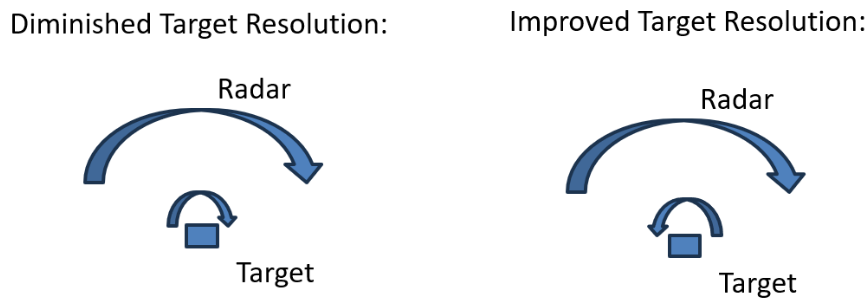

Figure 5.13: Rotational motion changes the effective aperture and therefore the achievable cross-range resolution. Rotation in the opposite direction of the radar improves resolution, whereas rotation in the same direction degrades resolution.

When the radar's rotation about the target and the target's rotation are in the same direction, the radar observes a smaller effective aperture on the target, diminishing cross-range resolution. On the contrary, opposing rotation rates increase the target's aperture, thereby improving the cross-range achievable resolution. To fairly compare the sharpness of different hypotheses, this change in effective resolution must be accounted for in the image grid cross-range width and pixel spacing.

It was observed while testing different hypotheses that the stationary clutter begins to contract or expand in the cross-range direction along with the target. This clutter appears to defocus with increasingly incorrect rotation rates, but initially the change is small enough that it just appears to stretch or compress the image.

This effect on cross-range was observed when attempting to focus a vehicle that was rotating on a turntable during the OU SAR collect. The phenomenon described can be seen in figures 5.14, 5.15, and 5.16.

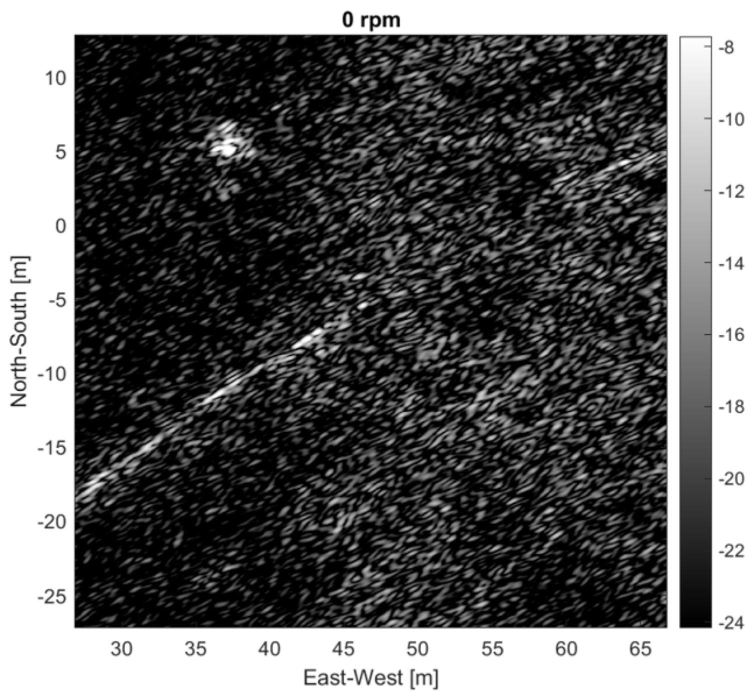

Figure 5.14: An unfocused image of a forklift on a turntable in the OU SAR collect. The target energy appears as a streak through the middle of the image. This was a standard backprojection image with no hypothesized ground motion.

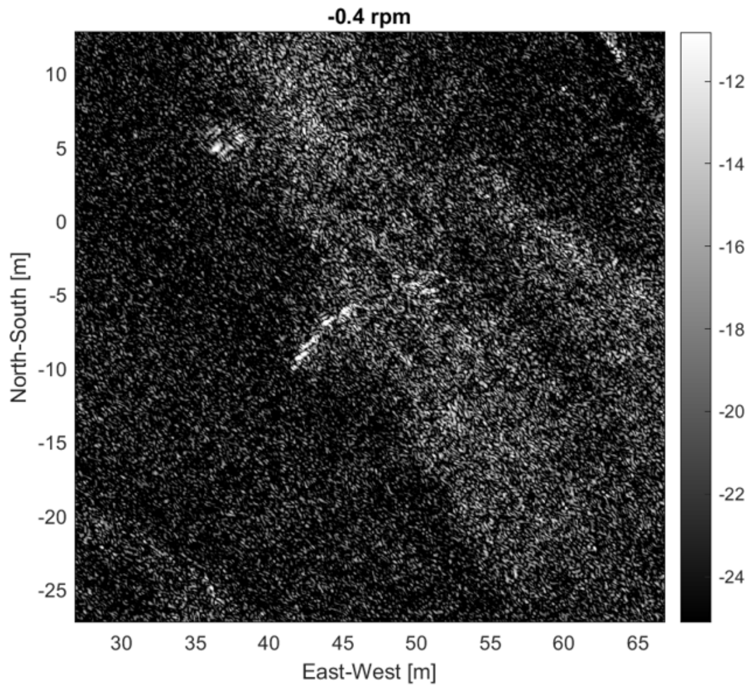

Figure 5.15: The hypothesized rotation pulls in energy from the surrounding scene in the cross-range direction.

Recall that the cross-range resolution is given by [3]

$$\rho_{CR} = \frac{\lambda_0}{2\theta_{SAR}}, \tag{5.5}$$

where θ_{SAR} is the angular change of the radar's perspective of some reference point (fig. 5.17). θ_{SAR} is typically viewed as a magnitude and left unsigned. However, the direction is needed to compensate for the changing resolution on the target.

Let θ_t be the signed change in angle experienced by a target on the ground during the aperture. This changes the size of the aperture made with the target. The new aperture angle will be called θ_{ISAR} From the target's perspective the radar's angular aperture will be

$$\theta_{ISAR} = \theta_{SAR} - \theta_t. \tag{5.6}$$

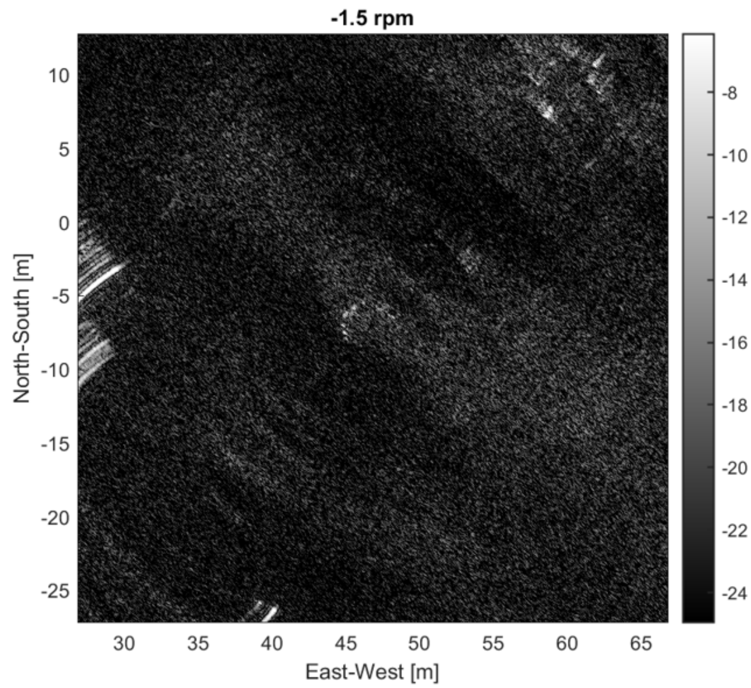

Figure 5.16: The target scatterers begin to take a form in the center of the image that more closely represents the target dimensions. However, the energy that gets pulled in from the scene is biasing the sharpness metric.

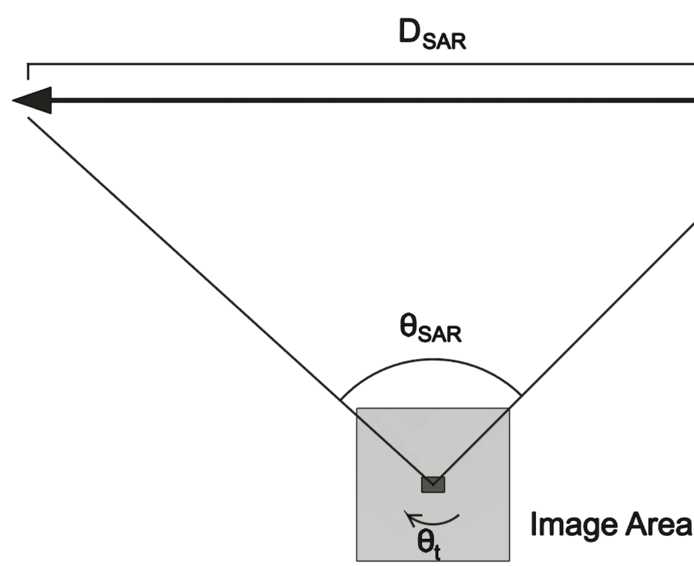

Figure 5.17: 2-D view of a SAR scenario where there is target rotation defined as θ_t.

The new cross-range resolution ρ'_{CR} is calculated as

$$\rho'_{CR} = \frac{\lambda_0}{2\theta_{ISAR}}. \tag{5.7}$$

The ratio of the new resolution to the old is used to scale the cross-range extent and resolution in the new image generated with that ISAR hypothesis. The scale factor κ_{CR} is given by

$$\begin{aligned} \kappa_{CR} &= \frac{\rho'_{CR}}{\rho_{CR}} \\ &= \frac{\theta_{SAR}}{\theta_{ISAR}}. \end{aligned} \tag{5.8}$$

In a three-dimensional SAR geometry, an accurate comparison requires θ_{SAR} and θ_t to be projected onto the same plane (fig. 4.1). First, project the two vectors that define the beginning and end of the antenna aperture onto the image plane. The angle between these two vectors (θ'_{SAR}) will be used to compare with the aperture made from the target rotation. This angle is only used to calculate the new scale factor. The scale factor now becomes

$$\kappa_{CR} = \frac{\theta'_{SAR}}{\theta'_{ISAR}} = \frac{\theta'_{SAR}}{\theta'_{SAR} - \theta_t}, \tag{5.9}$$

which is used to directly scale the cross-range extent (L_{CR}) and the cross-range resolution (ρ_{CR}) from the original image. This scale factor is necessary for an unbiased comparison of target focus. The scaled parameters become

$$\begin{aligned} L'_{CR} &= \kappa_{CR} L_{CR} \\ \rho'_{CR} &= \kappa_{CR} \rho_{CR}. \end{aligned} \tag{5.10}$$

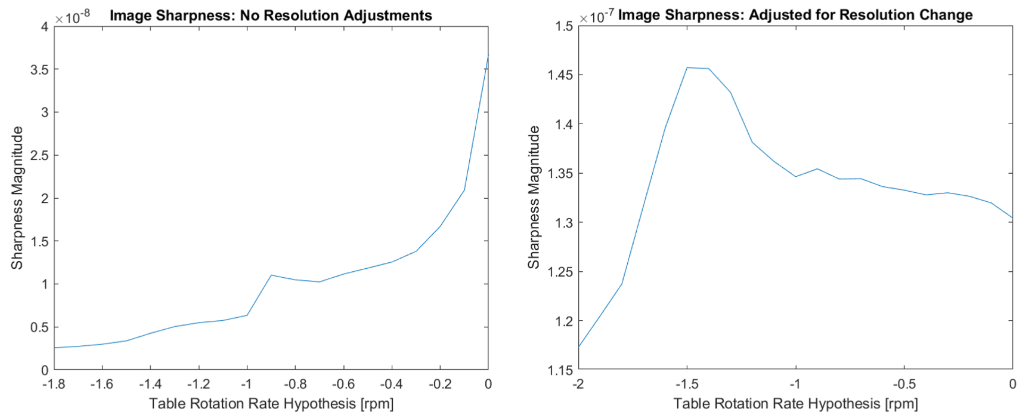

Figure 5.18: Measured sharpness for the turntable vehicle with and without the correct cross-range scaling.

Without the proper application of this scale factor, the image sharpness cannot be compared. The cross-range stretching or compression skews the sharpness measurement. Applying this scale factor keeps the image extent aligned with the hypothesized target aperture, preventing surrounding clutter from increasing the measured sharpness. Applyng the scale factor also keeps the target energy dispersed over approximately the same number of pixels. When applied to the real vehicle on the turntable, the peak correctly appeared at -1.5 [rpm] (fig. 5.18).

The scale factor approaches infinity as the hypothesized rotation rate nears the value that cancels the radar's rotation around the target (fig. 5.19). In this case, the aperture is effectively zero, and there is no cross-range resolution on the target. This causes a significant drop in measured sharpness at that rotation rate (fig. 5.20).

A rotating target will have mirrored rotation hypotheses that produce focused images [37]. A search over rotation rates when the target translational motion has been compensated reveals that the target focuses for both a positive and a corresponding negative hypothesized rotation rate (Fig. 5.20). This ambiguity limits what can be known about the target's motion but reduces the search to one side of the singularity.

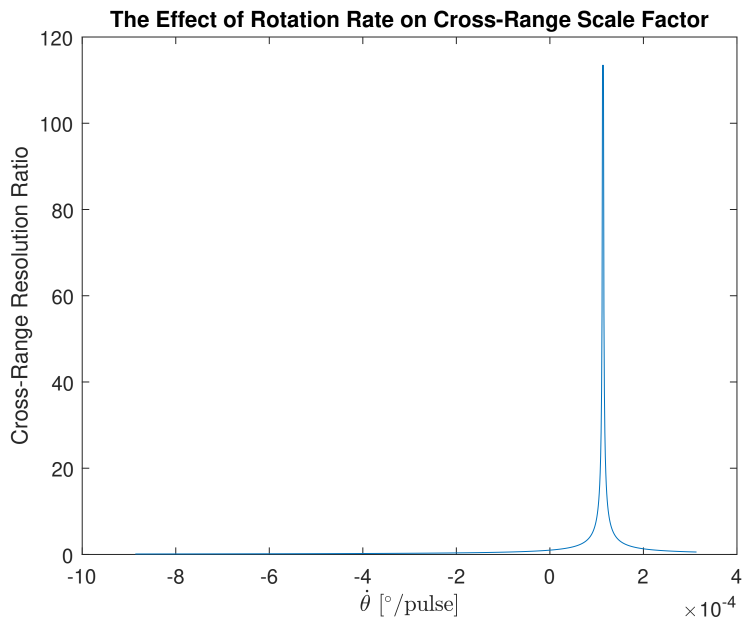

Figure 5.19: The computed cross-range scale factor, κ_{CR}, as a function of hypothesized rotation rate.

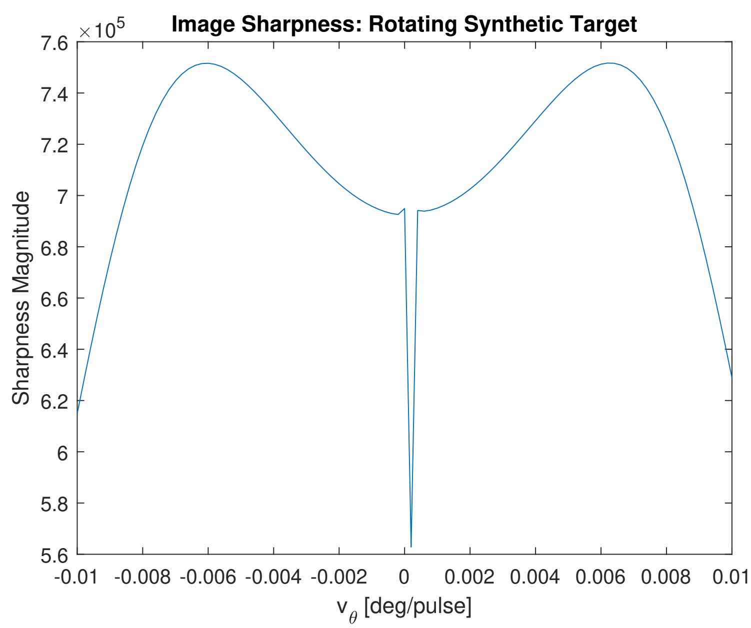

Figure 5.20: Measured image sharpness as a function of hypothesized rotation rates with κ_{CR} applied to resolution and cross-range image width.

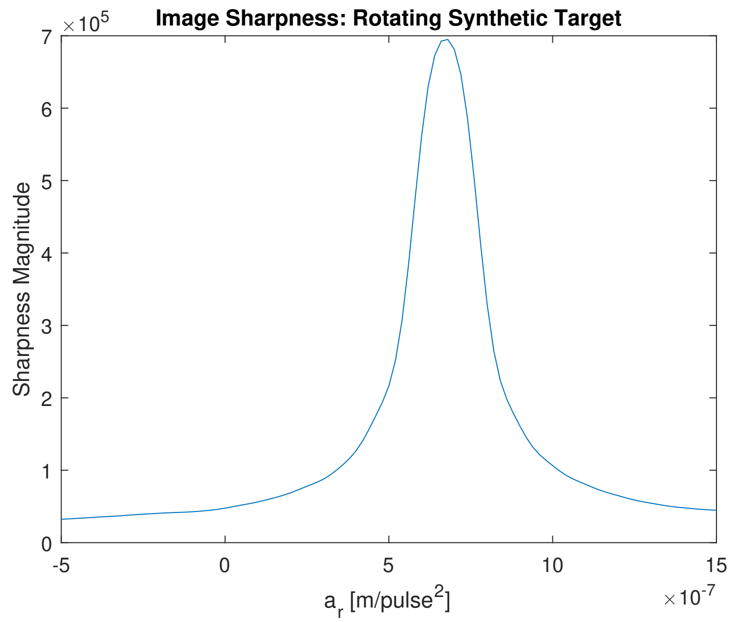

Figure 5.21: Measured image sharpness as a function of radial acceleration

5.4 Combined Parameter Search

The previous analysis has shown that the search can be limited to range acceleration and rotation rate. Image sharpness was evaluated as a function of rotational velocity and radial acceleration using the appropriate cross-range scale factor (Fig. 5.22). These parameters produce a vertically aligned ridge along a constant range acceleration.

Toward the top and bottom of the sharpness surface, four distinct ridges branch from the main ridge. Each of the branches corresponds to a continuum of motion hypotheses that can focus one of the four scatterers that constitute the rigid-body target (Figs. 5.23, 5.24). These branches represent ambiguities associated with individual scatterers, but they are resolved when the target is treated as a distributed object. A larger distributed target exhibits fewer ambiguities than a smaller target.

The main ridge lies along a constant range acceleration. The zero-rotation slice

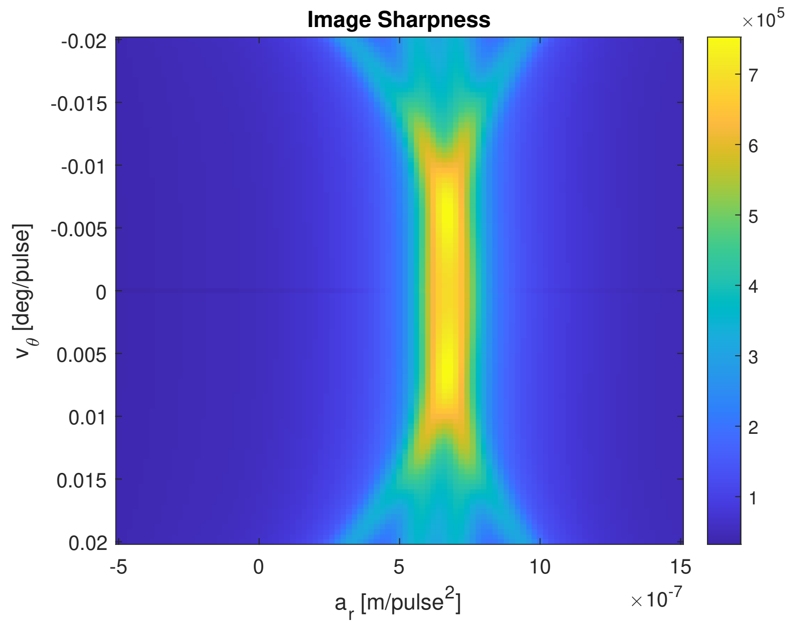

Figure 5.22: Image Sharpness as a function or range acceleration and rotation rate. Sharpness is approximately symmetric about the scale-factor singularity.

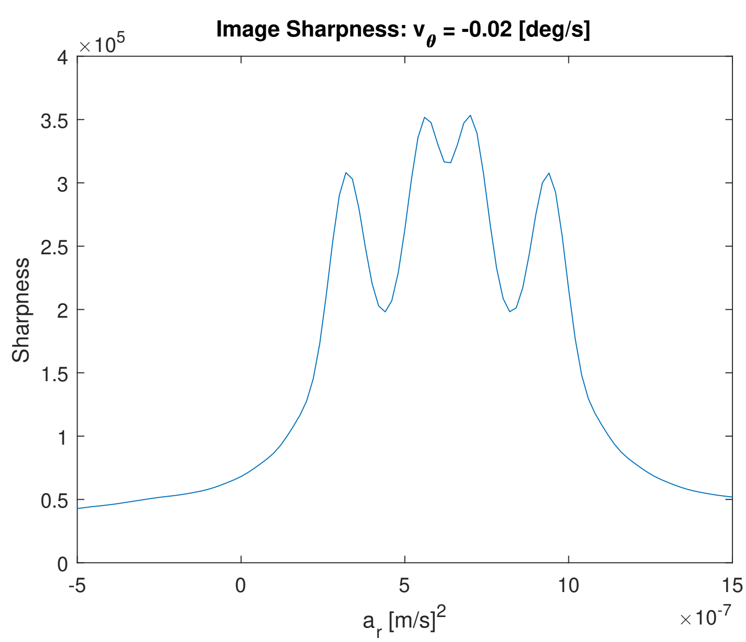

Figure 5.23: A slice of the sharpness surface showing four peaks that correspond to distinct hypotheses that individually focus each of the four scatterers.

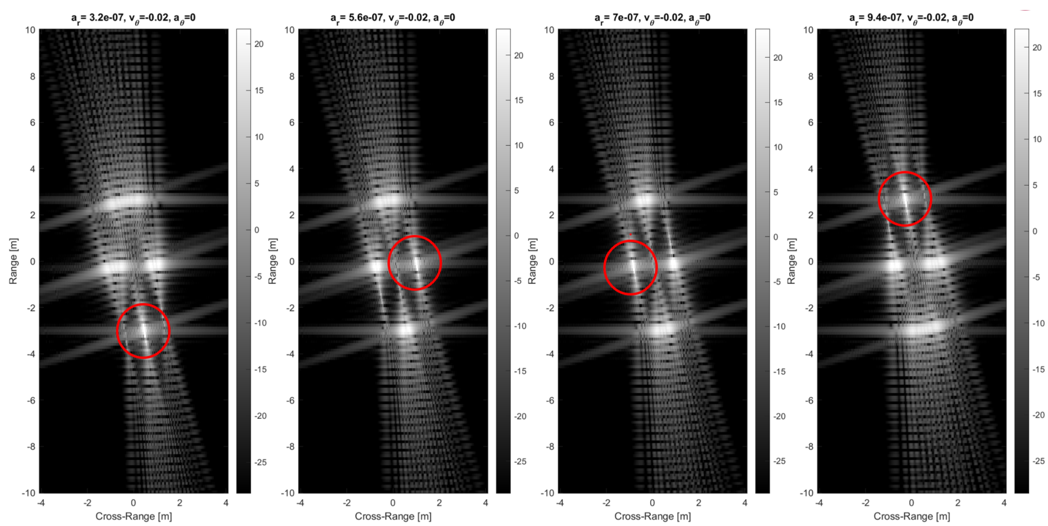

Figure 5.24: Each image focuses one of the scatterers on the target while leaving the rest smeared. The parameters correspond to the peak locations shown in Fig. 5.23.

reaches its maximum when the approximate range profile has been matched using the correct range acceleration (Fig. 5.21). Searching along the ridge reveals the sharpness global maximum (Fig. 5.20). The resulting image of the target discussed in Section 5.1.1 is shown in Figure 5.25. This image can be compared with the truth image for the same 1000 pulses in Figure 5.26. The autofocused image matches the size of the distributed target. This indicates that the RMC and cross-range scaling have been properly applied. The scatterers are well focused, although slight defocusing is observable. The autofocused image is less sharp than the truth image, which may result from the target's non-constant range acceleration and rotational velocity.

The autofocus algorithm was applied to the MiLa vehicle on 4000 pulses of the OU SAR dataset. The unfocused image of the vehicle shows the target energy smeared over at least 40 meters in cross-range (Fig. 5.27). After the TMC step, there is a noticeable reduction in cross-range smearing, but the target still appears

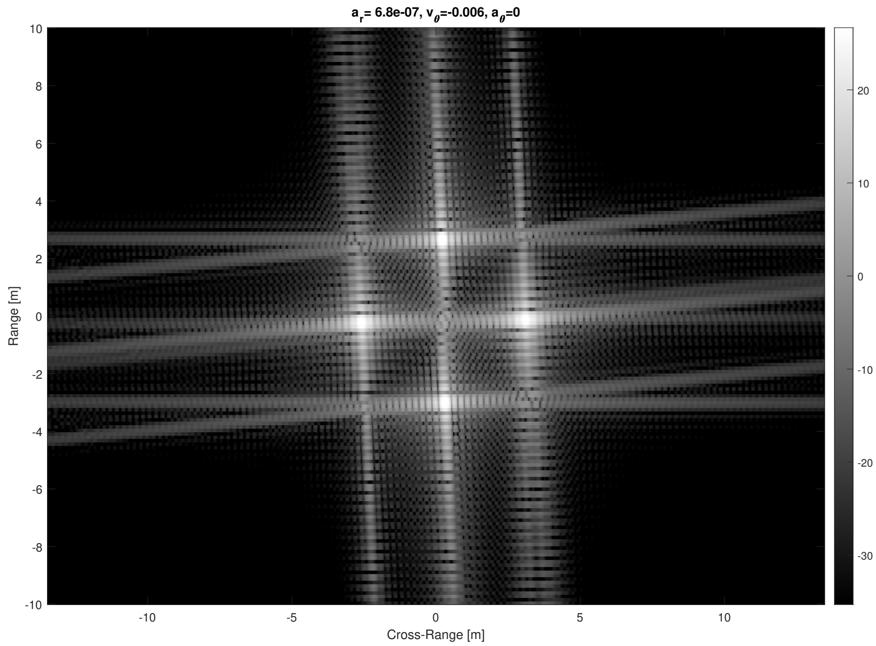

Figure 5.25: Autofocused image of the distributed scatterer target for 1000 pulses.

unfocused (Fig. 5.28). Because the GNSS data is insufficient to produce a truth image for the MiLa vehicle, it is difficult to verify that the vehicle has properly focused; however, after RMC the target appears focused and exhibits dimensions consistent with those of a car.

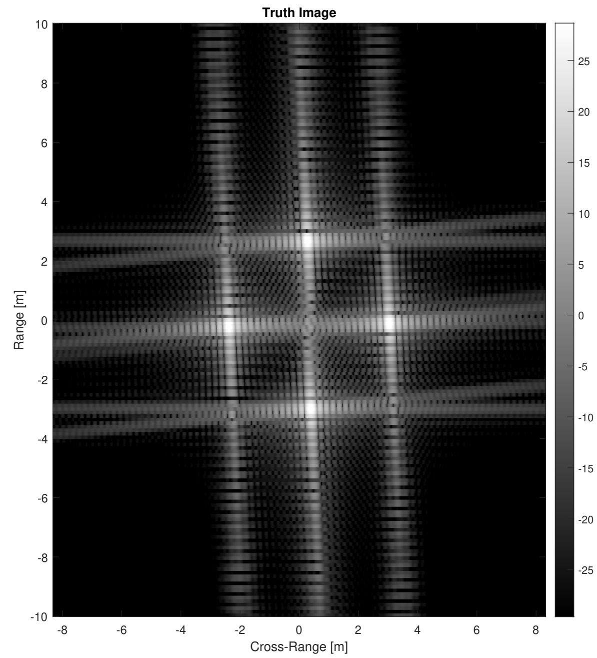

Figure 5.26: Truth image of the distributed scatterer target for 1000 pulses.

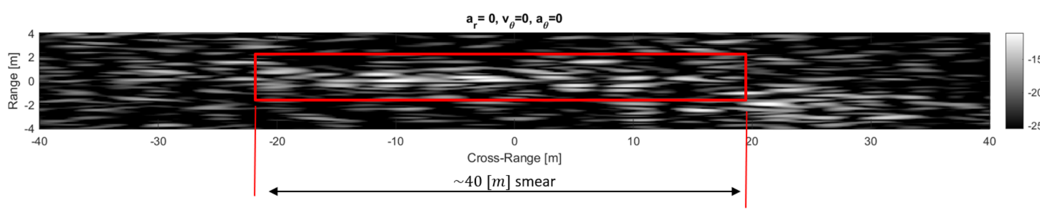

Figure 5.27: Unfocused image of the MiLa vehicle over 4000 pulses.

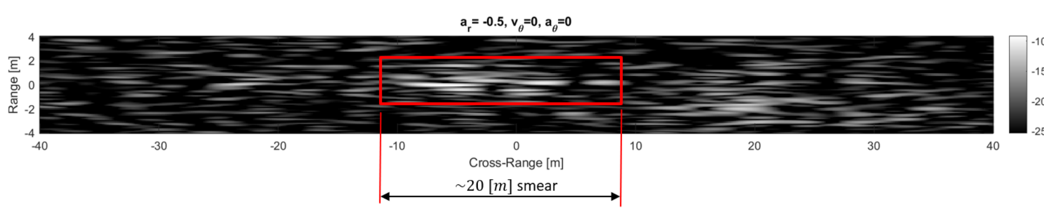

Figure 5.28: Image of MiLa vehicle after TMC.

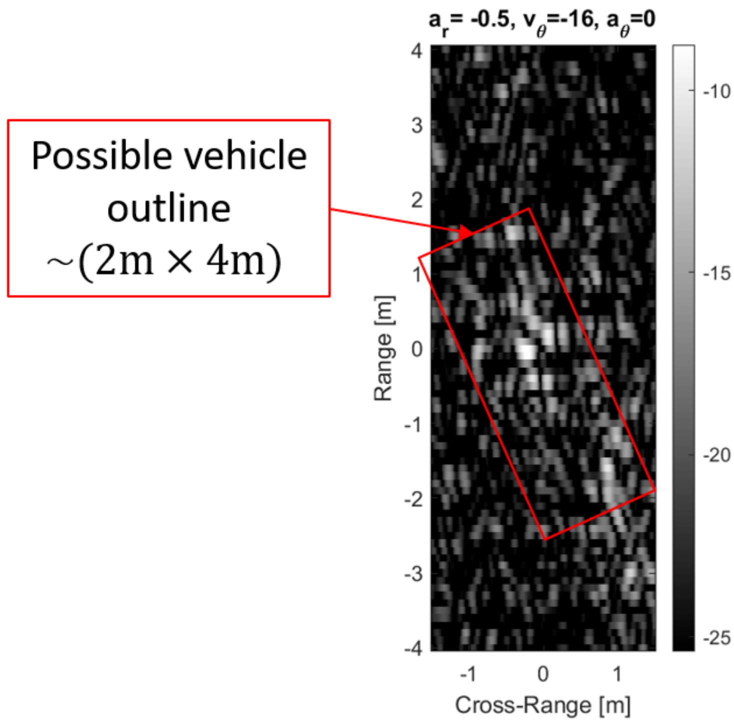

Figure 5.29: Image of MiLa vehicle after TMC and RMC.

Chapter 6

Conclusion

6.1 Conclusions

A backprojection-based ISAR parametric autofocus algorithm utilizing an image sharpness metric has been developed and successfully demonstrated on both simulated and real SAR data. A method for scaling the cross-range dimension of the image grid was also developed, enabling the evaluation of image sharpness over hypothesized rotation rates. The analysis performed during the development of this algorithm also revealed ambiguities in target motion hypotheses. It was observed that the range profile present in the data is largely insensitive to the specific combinations of target ground motion that generate it. As a result, the search space has been reduced to range acceleration and rotation rate. While the ambiguities help simplify the search, they also complicate reconstruction of the target's true ground motion.

6.2 Future Work

Several avenues for future work should be explored. The proposed algorithm has demonstrated successful focusing over short CPIs. Next, it should be investigated whether the target can be focused on subsequent CPIs to construct a piecewise approximation of the target's entire range profile. Such an approximation would enable image formation over longer aperture times and the generation of SAR videos. Additional analysis should investigate methods for decoupling range acceleration from cross-range velocity to reduce motion ambiguity.

Bibliography

[1] S. Werness, W. Carrara, L. Joyce, and D. Franczak, "Moving target imaging algorithm for sar data," *IEEE Transactions on Aerospace and Electronic Systems*, vol. 26, no. 1, pp. 57–67, 1990.

[2] T. Calloway and G. Donohoe, "Subaperture autofocus for synthetic aperture radar," *IEEE Transactions on Aerospace and Electronic Systems*, vol. 30, no. 2, pp. 617–621, 1994.

[3] M. Richards, *Fundamentals of Radar Signal Processing*, ser. McGraw-Hill education. McGraw-Hill, 2014. [Online]. Available: https://books.google.com/books?id=t_V5xAEACAAJ

[4] W. Carrara, R. Goodman, and R. Majewski, *Spotlight Synthetic Aperture Radar: Signal Processing Algorithms*, ser. Artech House remote sensing library. Artech House, 1995. [Online]. Available: https://books.google.com/books?id=uztiQgAACAAJ

[5] P. H. Eichel and C. V. Jakowatz, "Phase-gradient algorithm as an optimal estimator of the phase derivative." *Optics letters*, vol. 14 20, pp. 1101–3, 1989. [Online]. Available: https://api.semanticscholar.org/CorpusID:1584589

[6] V. Chen and M. Martorella, *Inverse Synthetic Aperture Radar Imaging: Principles, Algorithms and Applications*, ser. Electromagnetics and Radar. Institution of Engineering and Technology, 2014. [Online]. Available: https://books.google.com/books?id=xWmABAAAQBAJ

[7] "Ieee standard for radar definitions," *IEEE Std 686-2017 (Revision of IEEE Std 686-2008)*, pp. 1–54, 2017.

[8] R. Vehmas and N. Neuberger, "Inverse synthetic aperture radar imaging: A historical perspective and state-of-the-art survey," *IEEE Access*, vol. 9, pp. 113 917–113 943, 2021.

[9] C.-C. Chen and H. C. Andrews, "Target-motion-induced radar imaging," *IEEE Transactions on Aerospace and Electronic Systems*, vol. AES-16, no. 1, pp. 2–14, 1980.

[10] M. J. Prickett and C. C. Chen, “Principles of inverse synthetic aperture radar /ISAR/ imaging,” in *EASCON 1980; Electronics and Aerospace Systems Conference*, Jan. 1980, pp. 340–345.

[11] T. Itoh, H. Sueda, and Y. Watanabe, “Motion compensation for isar via centroid tracking,” *IEEE Transactions on Aerospace and Electronic Systems*, vol. 32, no. 3, pp. 1191–1197, 1996.

[12] L. Xi, L. Guosui, and J. Ni, “Autofocusing of isar images based on entropy minimization,” *IEEE Transactions on Aerospace and Electronic Systems*, vol. 35, no. 4, pp. 1240–1252, 1999.

[13] H.-s. Liao, G.-q. Hu, J.-b. Xiang, and S.-b. Peng, “A fast range alignment approach for isar imaging based on minimum entropy criterion,” in *2007 1st Asian and Pacific Conference on Synthetic Aperture Radar*, 2007, pp. 189–191.

[14] J. Wang and X. Liu, “Improved global range alignment for isar,” *IEEE Transactions on Aerospace and Electronic Systems*, vol. 43, no. 3, pp. 1070–1075, 2007.

[15] D. Zhu, L. Wang, Y. Yu, Q. Tao, and Z. Zhu, “Robust isar range alignment via minimizing the entropy of the average range profile,” *IEEE Geoscience and Remote Sensing Letters*, vol. 6, no. 2, pp. 204–208, 2009.

[16] D. Wahl, P. Eichel, D. Ghiglia, and C. Jakowatz, “Phase gradient autofocus-a robust tool for high resolution sar phase correction,” *IEEE Transactions on Aerospace and Electronic Systems*, vol. 30, no. 3, pp. 827–835, 1994.

[17] R. P. Bocker, T. B. Henderson, S. A. Jones, and B. R. Frieden, “New inverse synthetic aperture radar algorithm for translational motion compensation,” in *Stochastic and Neural Methods in Signal Processing, Image Processing, and Computer Vision*, S.-S. Chen, Ed., vol. 1569, International Society for Optics and Photonics. SPIE, 1991, pp. 298 – 310. [Online]. Available: https://doi.org/10.1117/12.48388

[18] F. Berizzi and G. Corsini, “Autofocusing of inverse synthetic aperture radar images using contrast optimization,” *IEEE Transactions on Aerospace and Electronic Systems*, vol. 32, no. 3, pp. 1185–1191, 1996.

[19] G. Delisle and H. Wu, “Moving target imaging and trajectory computation using isar,” *IEEE Transactions on Aerospace and Electronic Systems*, vol. 30, no. 3, pp. 887–899, 1994.

[20] R. Vehmas, J. Jylhä, M. Väilä, J. Vihonen, and A. Visa, “Data-driven motion compensation techniques for noncooperative isar imaging,” *IEEE Transactions on Aerospace and Electronic Systems*, vol. 54, no. 1, pp. 295–314, 2018.

[21] V. C. Chen, “Reconstruction of inverse synthetic aperture radar image using adaptive time-frequency wavelet transform,” in *Wavelet Applications II*, H. H. Szu, Ed., vol. 2491, International Society for Optics and Photonics. SPIE, 1995, pp. 373 – 386. [Online]. Available: https://doi.org/10.1117/12.205404

[22] F. Berizzi, E. Mese, M. Diani, and M. Martorella, “High-resolution isar imaging of maneuvering targets by means of the range instantaneous doppler technique: modeling and performance analysis,” *IEEE Transactions on Image Processing*, vol. 10, no. 12, pp. 1880–1890, 2001.

[23] R. Lipps and D. Kerr, “Polar reformatting for isar imaging,” in *Proceedings of the 1998 IEEE Radar Conference, RADARCON’98. Challenges in Radar Systems and Solutions (Cat. No.98CH36197)*, 1998, pp. 275–280.

[24] M. Martorella, F. Berizzi, and B. Haywood, “Contrast maximisation based technique for 2-d isar autofocusing,” *IEE Proceedings - Radar, Sonar and Navigation*, vol. 152, pp. 253–262, 2005. [Online]. Available: https://digital-library.theiet.org/doi/abs/10.1049/ip-rsn%3A20045123

[25] A. D. Lazarov and C. N. Minchev, “Isar signal modeling and image reconstruction with entropy minimization autofocussing,” in *2006 ieee/aiaa 25TH Digital Avionics Systems Conference*, 2006, pp. 1–11.

[26] J. Wang and X. Liu, “Sar minimum-entropy autofocus using an adaptive-order polynomial model,” *IEEE Geoscience and Remote Sensing Letters*, vol. 3, no. 4, pp. 512–516, 2006.

[27] M. Soumekh, *Synthetic Aperture Radar Signal Processing with MATLAB Algorithms*. Wiley, 1999. [Online]. Available: https://books.google.com/books?id=gVWqQgAACAAJ

[28] I. Cumming and F. Wong, *Digital Processing of Synthetic Aperture Radar Data: Algorithms and Implementation*, ser. Artech House remote sensing library. Artech House, 2005, no. v. 1. [Online]. Available: https://books.google.com/books?id=e9xxQgAACAAJ

[29] L. A. Gorham and L. J. Moore, “Sar image formation toolbox for matlab,” in *Algorithms for Synthetic Aperture Radar Imagery XVII*, vol. 7699. SPIE, 2010, pp. 46–58.

[30] A. W. Doerry, E. E. Bishop, and J. A. Miller, "Basics of backprojection algorithm for processing synthetic aperture radar images," *Sandia Report SAND2016-1682, Unlimited Release*, vol. 59, 2016.

[31] A. W. Doerry, E. Bishop, J. Miller, V. Horndt, and D. Small, "Designing interpolation kernels for SAR data resampling," in *Radar Sensor Technology XVI*, K. I. Ranney and A. W. Doerry, Eds., vol. 8361, International Society for Optics and Photonics. SPIE, 2012, p. 83611D. [Online]. Available: https://doi.org/10.1117/12.918106

[32] Z. Huang, A. Liu, R. Zhang, L. Li, and J. Cai, "Along- and cross-track relocation for ground moving target in a squint multichannel sar system," *Sensors*, vol. 26, no. 11, 2026. [Online]. Available: https://www.mdpi.com/1424-8220/26/11/3372

[33] J. Fienup, "Detecting moving targets in sar imagery by focusing," *IEEE Transactions on Aerospace and Electronic Systems*, vol. 37, no. 3, pp. 794–809, 2001.

[34] R. Perry, R. DiPietro, and R. Fante, "Sar imaging of moving targets," *IEEE Transactions on Aerospace and Electronic Systems*, vol. 35, no. 1, pp. 188–200, 1999.

[35] R. A. Muller and A. Buffington, "Real-time correction of atmospherically degraded telescope images through image sharpening," *J. Opt. Soc. Am.*, vol. 64, no. 9, pp. 1200–1210, Sep 1974. [Online]. Available: https://opg.optica.org/abstract.cfm?URI=josa-64-9-1200

[36] M. Newey, G. R. Benitz, D. J. Barrett, and S. Mishra, "Detection and imaging of moving targets with limit sar data," *IEEE Transactions on Geoscience and Remote Sensing*, vol. 56, no. 6, pp. 3499–3510, 2018.

[37] J. L. Walker, "Range-doppler imaging of rotating objects," *IEEE Transactions on Aerospace and Electronic Systems*, vol. AES-16, no. 1, pp. 23–52, 1980.